Article

Cell

SIRT6 Is Responsible for More Efficient DNA Double-Strand Break Repair in Long-Lived Species

Graphical Abstract

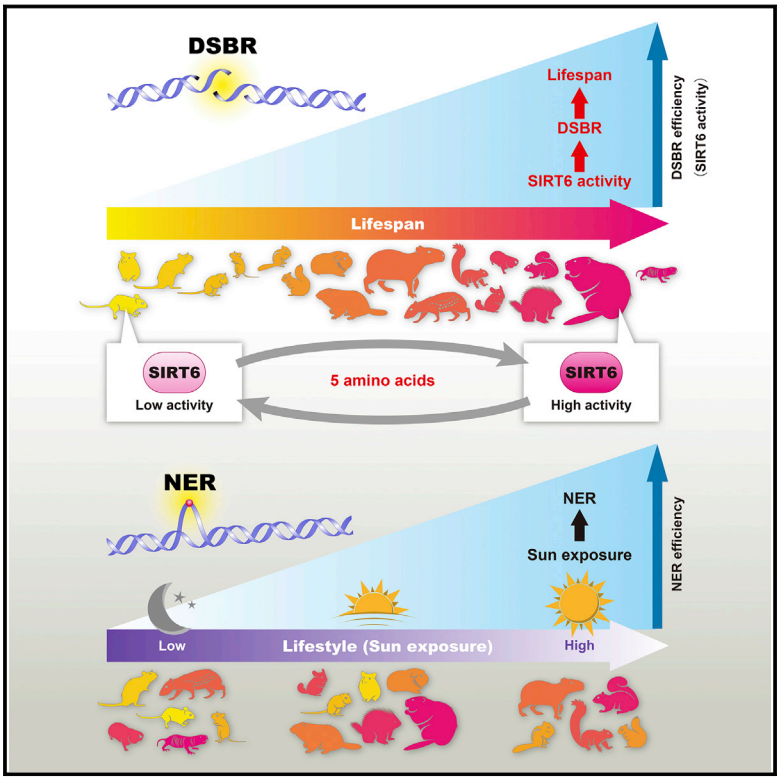

Highlights

- DSB repair, but not NER, coevolves with maximum lifespan (MLS) in rodents
- The activity of SIRT6 in stimulating DSB repair coevolves with MLS in rodent species
- Five amino acids determine the differential activities of mouse and beaver SIRT6
- Stronger SIRT6 leads to a longer lifespan

Authors

Xiao Tian, Denis Firsanov, Zhihui Zhang, ..., Vadim N. Gladyshev, Andrei Seluanov, Vera Gorbunova

Correspondence

andrei.seluanov@rochester.edu (A.S.), vera.gorbunova@rochester.edu (V.G.)

In Brief

A comparative analysis of 18 rodent species identifies a role for SIRT6-dependent DNA double strand break repair as a major factor in organismal lifespan

Tian et al., 2019, Cell *177*, 622–638
April 18, 2019
https://doi.org/10.1016/j.cell.2019.03.043

CellPress

Cell

Article

SIRT6 Is Responsible for More Efficient DNA Double-Strand Break Repair in Long-Lived Species

Xiao Tian,[1] Denis Firsanov,[1] Zhihui Zhang,[1] Yang Cheng,[2] Lingfeng Luo,[1] Gregory Tombline,[1] Ruiyue Tan,[1] Matthew Simon,[1] Steven Henderson,[1] Janine Steffan,[1] Audrey Goldfarb,[1] Jonathan Tam,[1] Kitty Zheng,[1] Adam Cornwell,[1] Adam Johnson,[1] Jiang-Nan Yang,[3] Zhiyong Mao,[4] Bruno Manta,[5] Weiwei Dang,[6] Zhengdong Zhang,[7] Jan Vijg,[7] Aaron Wolfe,[8] Kelsey Moody,[8] Brian K. Kennedy,[9,10] Dirk Bohmann,[2] Vadim N. Gladyshev,[5] Andrei Seluanov,[1,*] and Vera Gorbunova[1,11,*]

[1]Department of Biology, University of Rochester, Rochester, NY 14627, USA
[2]Department of Biomedical Genetics, University of Rochester Medical Center, Rochester, NY 14642, USA
[3]Leibniz Institute on Aging - Fritz Lipmann Institute, Beutenbergstraße 11, Jena D-07745, Germany
[4]School of Life Sciences and Technology, Tongji University, Shanghai 200092, China
[5]Division of Genetics, Department of Medicine, Brigham and Women's Hospital, Harvard Medical School, Boston, MA, USA
[6]Huffington Center on Aging, Department of Molecular and Human Genetics, Baylor College of Medicine, Houston, TX 77030, USA
[7]Department of Genetics, Albert Einstein College of Medicine, Bronx, NY, USA
[8]Ichor Therapeutics, 2521 US-11, Lafayette, NY 13084, USA
[9]Departments of Biochemistry and Physiology, National University Singapore, Singapore
[10]Centre for Healthy Aging, National University Health System, Singapore
[11]Lead Contact
*Correspondence: andrei.seluanov@rochester.edu (A.S.), vera.gorbunova@rochester.edu (V.G.)
https://doi.org/10.1016/j.cell.2019.03.043

SUMMARY

DNA repair has been hypothesized to be a longevity determinant, but the evidence for it is based largely on accelerated aging phenotypes of DNA repair mutants. Here, using a panel of 18 rodent species with diverse lifespans, we show that more robust DNA double-strand break (DSB) repair, but not nucleotide excision repair (NER), coevolves with longevity. Evolution of NER, unlike DSB, is shaped primarily by sunlight exposure. We further show that the capacity of the SIRT6 protein to promote DSB repair accounts for a major part of the variation in DSB repair efficacy between short- and long-lived species. We dissected the molecular differences between a weak (mouse) and a strong (beaver) SIRT6 protein and identified five amino acid residues that are fully responsible for their differential activities. Our findings demonstrate that DSB repair and SIRT6 have been optimized during the evolution of longevity, which provides new targets for anti-aging interventions.

INTRODUCTION

Maximum lifespan (MLS) differs up to 200-fold among mammals (Tacutu et al., 2013). However, the molecular mechanisms that are responsible for these dramatic differences are largely unknown. DNA repair has been hypothesized to play an important role in lifespan determination, as mutations in DNA repair genes result in phenotypes resembling accelerated aging (Hasty et al., 2003). For example, several human progeroid syndromes are associated with congenital mutations in genes involved in DNA double strand break (DSB) repair, such as Ataxia-telangiectasia (Shiloh and Lederman, 2017) and Werner syndrome (Oshima et al., 2017), and in nucleotide excision repair (NER), such as Cockayne syndrome (Karikkineth et al., 2017), Trichothiodystrophy (Faghri et al., 2008), and XPF-ERCC1 (XFE) progeroid syndrome (Niedernhofer et al., 2006). In mice, mutations in DSB repair genes such as *Ku70*, *Ku80*, and *Prkdc*, and NER genes such as *Ercc1* and *Xpd* shorten lifespan (reviewed in (Vermeij et al., 2016)). However, evidence linking improved DNA repair and longer lifespan is currently lacking, primarily because no approach has been developed to safely and efficiently augment DNA repair.

Natural selection has created mammals with dramatically diverse aging rates—a diversity that can be exploited to understand the mechanisms of aging and lifespan control through comparative biology. Previous studies have suggested that genomic maintenance mechanisms are involved in regulating lifespan. For example, cells from long-lived species show higher resistance to a variety of genotoxic stress (Harper et al., 2007; Kapahi et al., 1999). However, which DNA repair pathways are upregulated in long-lived species is less clear. It has been shown that DNA DSB repair efficiency declines with age (Garm et al., 2013; Vaidya et al., 2014), leading to accumulation of genomic rearrangements (Dollé et al., 2000), which are hallmarks of cancer and aging. It was also reported that nuclear extracts from long-lived species have higher DNA end binding activity (Lorenzini et al., 2009), suggesting enhanced NHEJ. Additionally, several studies have analyzed the relationship between NER and lifespan, with some reporting a positive correlation (Francis et al., 1981; Hart and Setlow, 1974) and others reporting no such relationship (Kato et al., 1980). This discrepancy is possibly due to improper accounting for the confounding effects of body mass

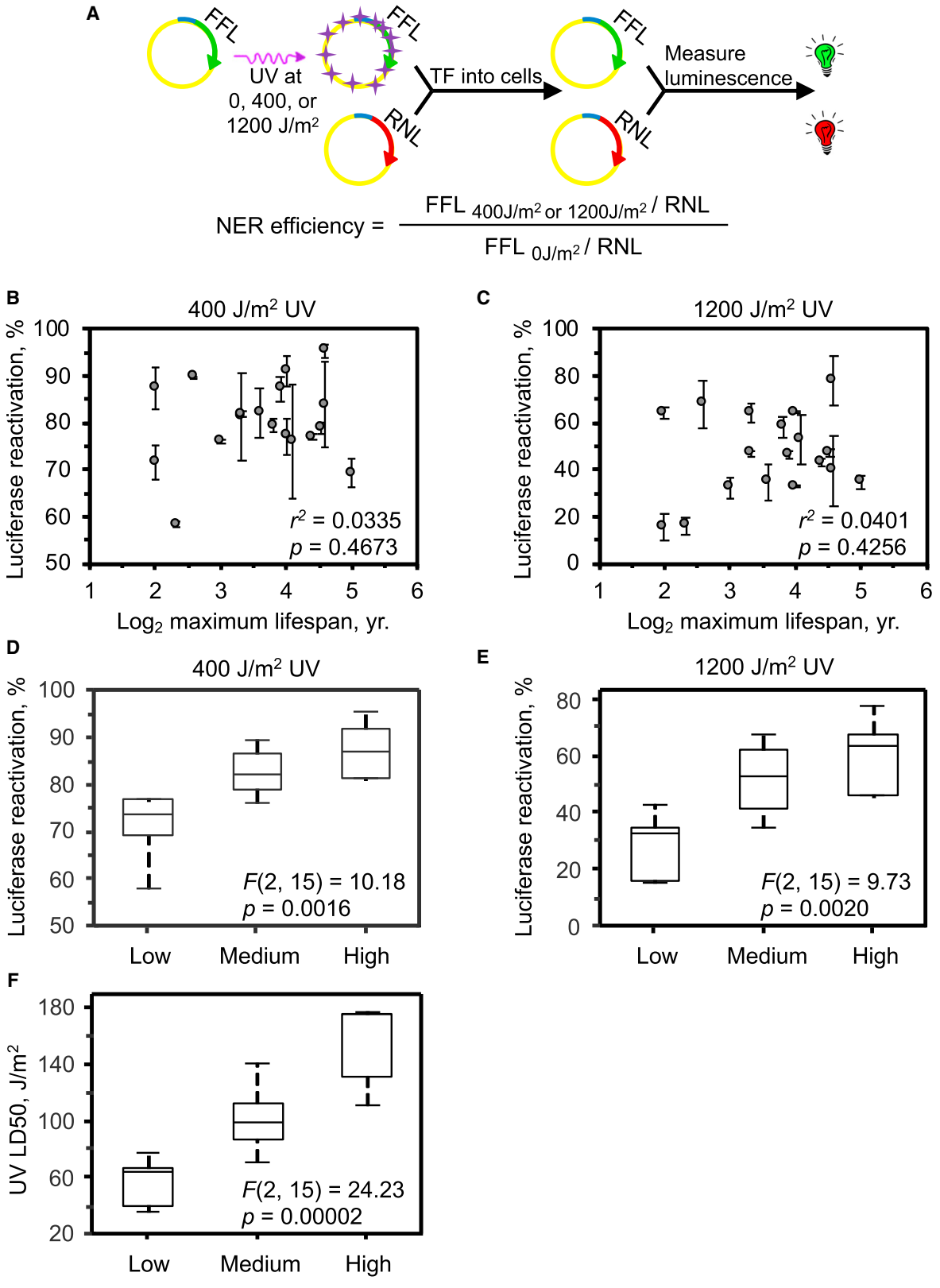

(legend on next page)

and phylogeny (Promislow, 1994). In this study, we aimed to understand how DNA repair pathways are regulated in long-lived species in order to maintain genomic stability.

DNA repair is regulated by DNA damage response genes and chromatin remodelers. *Sirt6* is one such gene that not only regulates DNA repair, but also maintains epigenomic stability and promotes longevity. Specifically, SIRT6 promotes base excision repair (Mostoslavsky et al., 2006) and both the homologous recombination (HR) and the non-homologous end joining (NHEJ) pathways of DSB repair (Mao et al., 2011; Toiber et al., 2013). Additionally, mice lacking *Sirt6* display genomic instability and a shorter lifespan (Mostoslavsky et al., 2006), while mice overexpressing *Sirt6* show lifespan extension (Kanfi et al., 2012). In this regard, SIRT6 may be a contributing factor for the evolution of longevity. Furthermore, the activity of PARP1, a downstream target of SIRT6 in DSB repair, correlates with species lifespan (Grube and Bürkle, 1992). However, it is not yet known if SIRT6 function is enhanced in long-lived species.

Rodents are an ideal group to pursue comparative aging studies (Gorbunova et al., 2014) because rodents are closely related phylogenetically, yet their MLS are extremely diverse. To determine whether long-lived species evolve more efficient DNA repair, we carried out a systematic analysis of DSB repair and NER in primary fibroblasts isolated from 18 species of rodents with MLS ranging from 3 years to 32 years (Figure S1).

RESULTS

NER Does Not Correlate with Species Maximum Lifespan or Body Mass

Genetic evidence links defects in NER and DSB repair to premature aging phenotypes. To test whether these DNA repair pathways are enhanced during the evolution of increased lifespan, we measured the efficiency of NER and DSB repair in a collection of 18 rodent species with diverse MLS (Figure S1).

NER removes bulky DNA adducts generated by ultraviolet light (UV) exposure such as thymidine dimers and 6,4-photoproducts. To quantify NER, we utilized a host cell reactivation assay (Figure 1A). Firefly luciferase (FFL) plasmid was treated with 254 nm UV radiation at 0, 400, or 1,200 J/m^2. Each FFL plasmid was then co-transfected with an intact Renilla luciferase (RNL) plasmid into low passage primary skin fibroblasts (population doubling [PD] < 10) isolated from 18 rodent species. Skin was chosen because it is the organ most exposed to sunlight. Importantly, the amount of both FFL and RNL plasmids were within a linear range that causes proportional change of luciferase activity (Figures S2A and S2B). The FFL plasmid undergoes repair by the cellular machinery, and the levels of luciferase activity are thus proportional to the repair capacity of the cells.

We observed large differences in the efficiency of repair of UV-induced damage between species (Figures 1B and 1C). For example, for 1200 J/m^2 UV-damaged plasmid, the successful repair ranged from 15.4% to 78.0% between species. Surprisingly, we observed no significant correlation between luciferase recovery and maximum lifespan (400 J/m^2, r^2 = 0.034, p = 0.47; 1200 J/m^2, r^2 = 0.040, p = 0.43) (Figures 1B and 1C) or body mass (400 J/m^2, r^2 = 0.048, p = 0.38; 1200 J/m^2, r^2 = 0.0053, p = 0.77) (Figures S2C and S2D). These results indicate that factors other than lifespan or body mass drive the evolution of NER.

Evolution of NER Efficiency Is Shaped by Sunlight Exposure

Since solar UV radiation is the major cause of DNA damage repaired by NER, we hypothesized that the level of sunlight exposure drives the evolution of NER. The rodent clade includes species with diverse ecology that experience different levels of sunlight exposure. So, to test this hypothesis, we divided the 18 rodent species in our collection into three groups based on environmental sunlight exposure: (1) the low-UV group included strictly nocturnal and subterranean species; (2) the medium-UV group included crepuscular species; and (3) the high-UV group which included diurnal species (Table S1). This classification revealed a significant difference in NER efficiency between the three UV groups (400 J/m^2, F[2, 15] = 10.18, p = 0.0016; 1200 J/m^2, F[2, 15] = 9.73, p = 0.0020) (Figures 1D and 1E). Phylogenetic ANOVA, which takes phylogeny into account in variance analysis (Revell, 2012), confirmed this significant difference (400 J/m^2, F[2, 15] = 10.18, p = 0.014; 1200 J/m^2, F[2, 15] = 9.73, p = 0.016). Post-hoc pairwise comparison tests indicated that NER efficiency of the low-UV species was significantly different from that of the medium-UV species (400 J/m^2, p = 0.013; 1200 J/m^2, p = 0.0098) and high-UV species (400 J/m^2, p = 0.018; 1200 J/m^2, p = 0.025). However, the difference between medium-UV and high-UV species was not significant (400 J/m^2, p = 0.36; 1200 J/m^2, p = 0.47). These results indicate that NER in low-UV species, though including species with a wide range of maximum lifespans of 4–32 years (Table S1), is significantly less efficient than that in sunlight-exposed species, including both medium- and high-UV species.

We next assessed if NER efficiency increases quantitatively with the level of sunlight exposure. Because it is impossible to

Figure 1. NER Efficiency Does Not Correlate with Maximum Lifespan in 18 Rodent Species

(A) Host cell reactivation assay to measure NER efficiency. NER efficiency was calculated as the percentage of the luciferase reactivation and the formula is shown.

(B, C) Luciferase reactivation of UV-damaged FFL plasmid at (B) 400 J/m^2 or (C) 1200 J/m^2 does not correlate with species MLS (also see Figure S2C, D for no correlation to body mass). Cells isolated from at least 3 different animals of each species were used and each circle represents a species. Error bars indicate SEM, *r*, Pearson correlation coefficient. p values were determined by t test.

(D and E) Luciferase reactivation of UV-damaged FFL plasmid at (D) 400 J/m^2 or (E) 1200 J/m^2 is significantly different across the three sunlight exposure groups. The data from Figures 1B and 1C were used to plot against the level of sunlight exposure. Classification of the three sunlight exposure groups was based on the lifestyle and habitat of the species (Table S1). Statistical significance was tested using one-way ANOVA. Data were phylogenetically corrected.

(F) UV LD50 is significantly different across the three sunlight exposure groups. One-way ANOVA was used to test statistical significance. Data were phylogenetically corrected.

See also Table S1 and Figures S1 and S2.

accurately quantify species sunlight exposure, we performed Spearman's rank correlation tests. Luciferase recovery showed significant correlation with sunlight (400 J/m^2, r_S = 0.77, p = 0.0002; 1200 J/m^2, r_S = 0.74, p = 0.0004) (Figures S2E and S2F). The correlation remained significant after correction for phylogenetic non-independence by the method of independent contrasts (Felsenstein, 1985) (400 J/m^2, r_S = 0.71, p = 0.0010; 1200 J/m^2, r_S = 0.67, p = 0.0022). Collectively, these data indicate that environmental UV exposure, but not MLS, drives the evolution of NER.

We then asked if the differences observed in NER efficiency contribute to cell survival. Low-passage fibroblasts (PD < 10) from rodent species were subjected to serial doses of UV radiation and cell survival was measured 3 days later using a WST-1 assay (Harper et al., 2007). We found no significant correlation between LD50 and maximum lifespan (r^2 = 0.060; p = 0.33) or adult body mass (r^2 = 0.019; p = 0.59) (Figures S2G and S2H). However, LD50 exhibited a significant difference across the three UV groups (F[2, 15] = 24.23, p < 0.0001; Figure 1F). Phylogenetic ANOVA confirmed this significant difference (F[2, 15] = 24.23, p = 0.0002). Post-hoc testing revealed that all three groups are significantly different from each other (low-UV versus medium-UV, p = 0.0046; low-UV versus high-UV, p = 0.00039; medium-UV versus high-UV, p = 0.0087). Quantitatively, UV LD50 positively correlated with the level of sunlight exposure tested with Spearman's rank correlation (r_S = 0.87, p < 0.0001; Figure S2I), which remained significant after correction for phylogenetic non-independence (r_S = 0.77, p = 0.0002). These results demonstrate that cells from UV-exposed species evolved higher resistance to UV radiation. Moreover, cell survival correlated with luciferase recovery of 1,200 J/m^2 UV-damaged FFL plasmid (r^2 = 0.47, p = 0.0017; Figure S2J), which remained significant after correction for phylogenetic non-independence (r^2 = 0.33, p = 0.013), indicating that UV resistance of high-UV species is mediated, at least in part, by the more efficient NER.

DNA DSB Repair Coevolves with Longevity

We next tested if DNA DSB repair coevolves with MLS. DNA DSBs are repaired by two major pathways: non-homologous end joining (NHEJ) and homologous recombination (HR). We measured the efficiency of NHEJ and HR repair using GFP-based reporters (Mao et al., 2011) (Figures 2A–2C). The reporter constructs were integrated into the genome of early passage (PD < 10) primary skin and lung fibroblasts. To avoid bias due to position effect, the DSB repair efficiency was measured in a pool of at least 100 independent clones for each cell line.

DSB repair by NHEJ (Figure S3A) showed a strong positive correlation with species maximum lifespan in both skin (r^2 = 0.76, p < 0.0001; Figure 2D) and lung fibroblasts (r^2 = 0.59, p = 0.0008; Figure 2E), but not with body mass (skin fibroblasts: r^2 = 0.13, p = 0.19; lung fibroblasts: r^2 = 0.15, p = 0.15; Figures S3B and S3C). The correlation between NHEJ efficiency and lifespan remained significant after correction for phylogenetic non-independence by the method of independent contrasts (Felsenstein, 1985) (skin fibroblasts: r^2 = 0.57, p = 0.0012; lung fibroblasts: r^2 = 0.31, p = 0.033).

DSB repair by HR (Figure S3D) also showed a very strong positive correlation with species maximum lifespan in both skin (r^2 = 0.76, p < 0.0001; Figure 2F) and lung fibroblasts (r^2 = 0.65, p = 0.0002; Figure 2G). This correlation also remained significant after correction for phylogenetic non-independence (skin fibroblasts: r^2 = 0.59, p = 0.0008; lung fibroblasts: r^2 = 0.32, p = 0.021). There was no significant correlation between HR repair efficiency and body mass of the species in skin fibroblasts (r^2 = 0.17, p = 0.12; Figure S3E). A significant correlation between HR repair efficiency and body mass was revealed in lung fibroblasts (r^2 = 0.36, p = 0.014; Figure S3F), but the significance was lost after correction for phylogenetic non-independence (r^2 = 0.17, p = 0.11). These results demonstrate that the efficiency of both pathways of DSB repair shows very strong positive correlations with species MLS.

We also tested DSB repair using alternative assays, including γ-H2AX and 53BP1 foci quantification and colony formation assay after γ-radiation (Figure S4A). We found that similar numbers of foci were induced 1 h after radiation among species (Figure S4B). However, fewer foci were observed in the cells from long-lived species than that from short-lived species after 24 h (Figures S4A and S4B), indicating that the long-lived species are more potent at resolving γ-radiation-induced DNA damage foci. Moreover, the number of unrepaired foci at 24 h showed a significant negative correlation with species maximum lifespan (Figure S4C), but not with body mass (Figure S4D), suggesting that stronger DNA repair is a property that co-evolved specifically with longevity. Importantly, the number of unrepaired foci at 24 h showed a very strong correlation with NHEJ efficiency (r^2 = 0.8131) measured using our reporter construct (Figure S4E), indicating that the DNA repair efficiency measured with the DNA repair reporter and the DNA damage foci agrees with each other.

We also performed colony formation assays in the skin fibroblasts from both short- and long-lived rodent species after γ-radiation and calculated their LD50 (Figures S4F and S4G). LD50 showed a significant positive correlation with species maximum lifespan (Figure S4H), but not with body mass (Figure S4I). The stronger resistance to γ-radiation in long-lived species is in line with our finding that long-lived species have more efficient DSB repair. Indeed, LD50 also showed a significant positive correlation with NHEJ efficiency (Figure S4J). Both the foci quantification and the colony formation data confirmed that long-lived species harbor more efficient DSB repair machinery than short-lived species.

Together, these data indicate that DSB repair, but not NER, coevolves with longevity.

SIRT6 Activity in Promoting DSB Repair Coevolves with Longevity

To understand the molecular mechanisms responsible for more efficient DSB repair in long-lived species, we sought to interrogate a DNA repair factor that acts upstream of the separation between NHEJ and HR pathways since both of these pathways are enhanced in long-lived species. SIRT6, a nuclear localized member of the sirtuin family, is such a factor, as it is an upstream regulator of both pathways of DSB repair (Mao et al., 2011; Toiber et al., 2013). Specifically, SIRT6 stimulates both NHEJ and HR repair when overexpressed (Mao et al., 2011). Therefore, we investigated whether SIRT6 mediates the coevolution of DSB repair and longevity.

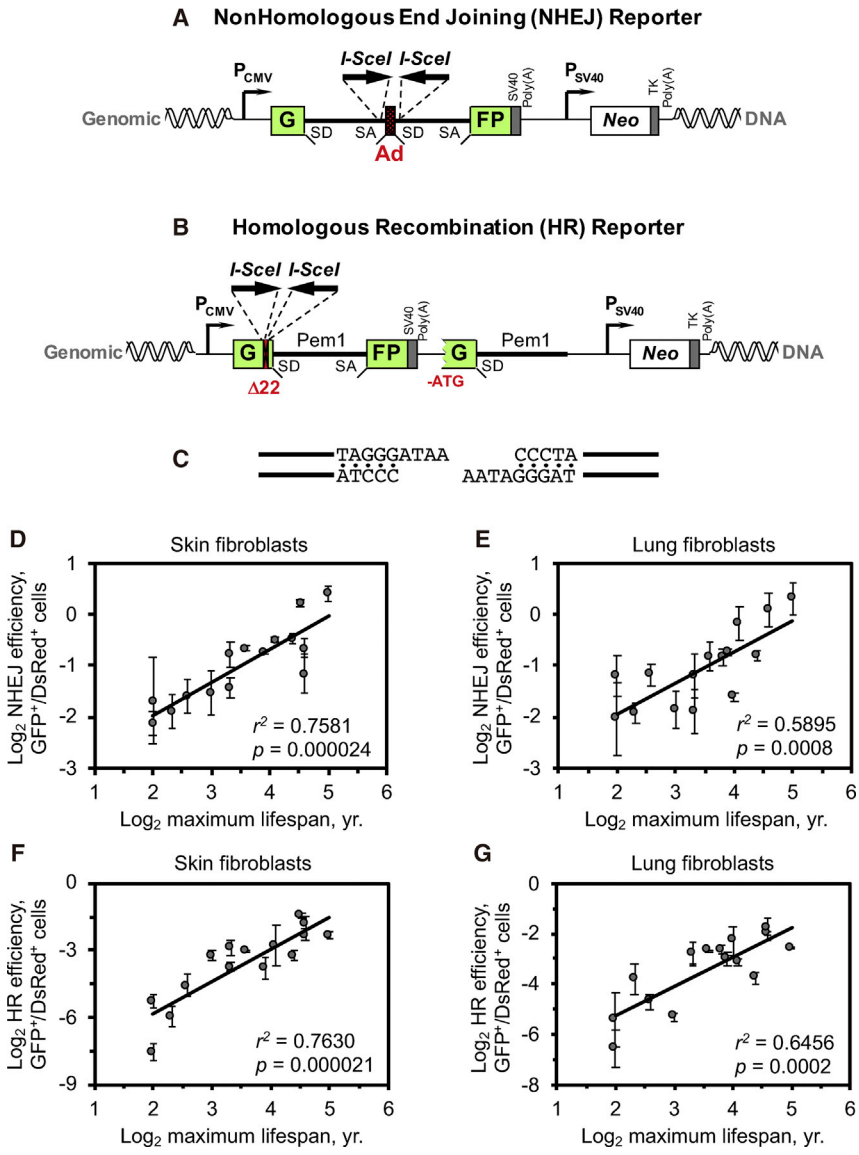

Figure 2. The Efficiency of DNA DSB Repair Positively Correlates with Maximum Lifespan

(A) NHEJ repair reporter construct. The GFP coding sequence containing an intron from the rat Pem1 gene is interrupted by an adenoviral exon (Ad). Splicing Ad into the GFP gene makes it inactive. Ad is flanked by I-SceI recognition sites in inverted orientation. Induction of a DSB by I-SceI enzyme followed by successful NHEJ reconstitutes a functional GFP gene. SD, splice donor; SA, splice acceptor.

(B) HR repair reporter construct. 22 nucleotides of the GFP coding sequence was replaced with two I-SceI recognition sites in inverted orientation. This 22 nt deletion ensures that GFP cannot be reconstituted by an NHEJ repair event. An HR repair template, which lacks the ATG start codon and the second exon of GFP, is placed after the GFP coding sequence. Induction of a DSB by I-SceI enzyme followed by a gene conversion event reconstitutes a functional GFP gene.

(C) DNA repair substrate. Two adjacent I-SceI cuts generate non-compatible DNA ends.

(D-G) NHEJ repair efficiency (D, E) and HR repair efficiency (F, G) correlate with species maximum lifespan. NHEJ and HR reporter constructs were integrated into primary, low passage skin and lung fibroblasts. DNA DSBs repair efficiency was assayed by transfecting cells with I-SceI expression vector and a DsRed plasmid as a transfection control (Seluanov et al., 2010a). The repair efficiency was calculated as the ratio of $GFP^+/DsRed^+$ cells. Experiments were repeated at least 3 times for each cell line. Cells from at least 3 animals were assayed for each species. Error bars represent SEM *r*, Pearson correlation coefficient. p values were determined by t test for the uncorrected data; the values for phylogenetically corrected data are shown in the text.

See also Figure S3, S4.

As the sequences of most *Sirt6* genes from the studied rodent species were unknown, we cloned their *Sirt6* cDNAs by rapid amplification of cDNA ends (RACE). The alignment of rodent SIRT6 proteins revealed that the C-terminal region is highly divergent between species (Figures 3A and 3B).

We then tested the activity of SIRT6 from different species in stimulating DSB repair. We chose to conduct the assay in mouse cells carrying a chromosomally integrated NHEJ reporter construct because mouse is the shortest-lived among our species set and mouse cells had a low level of NHEJ activity. The fold of stimulation by SIRT6 is calculated by the ratio of DSB repair efficiency with SIRT6 overexpression to that with the overexpression of a control plasmid (Figure 4A). We found that the ability of SIRT6 to stimulate NHEJ repair correlates strongly with MLS of the rodents (r^2 = 0.54, p = 0.0008; Figure 4B), but not with body mass (r^2 = 0.19, p = 0.078; Figure S5A). The correlation between SIRT6-mediated stimulation of NHEJ and lifespan remained significant after correction for phylogenetic non-independence (r^2 = 0.34, p = 0.014).

Next, we tested stimulation of HR repair by SIRT6 from different species. This was measured in rat cells because HR repair efficiency in mouse adult fibroblast was extremely low using our construct (Figure S3D), which does not allow a reliable assessment of SIRT6's effect on HR repair due to high variation in measuring such rare events. Similar to NHEJ, we found that SIRT6 activity in stimulating HR repair correlates significantly with MLS (r^2 = 0.64, p = 0.0001; Figure 4C). This correlation remained significant after correction for phylogenetic non-independence (r^2 = 0.40, p = 0.006). There was a significant correlation between SIRT6 activity in promoting HR and body mass (r^2 = 0.32, p = 0.018; Figure S5B), but this correlation was lost after phylogenetic correction (r^2 = 0.17, p = 0.10). These results suggest that SIRT6 activity in promoting DSB repair coevolves with longevity. Since SIRT6 is involved in regulating both pathways of DSB repair (Mao et al., 2011), we calculated the contribution of SIRT6 to the correlation between DSB repair and

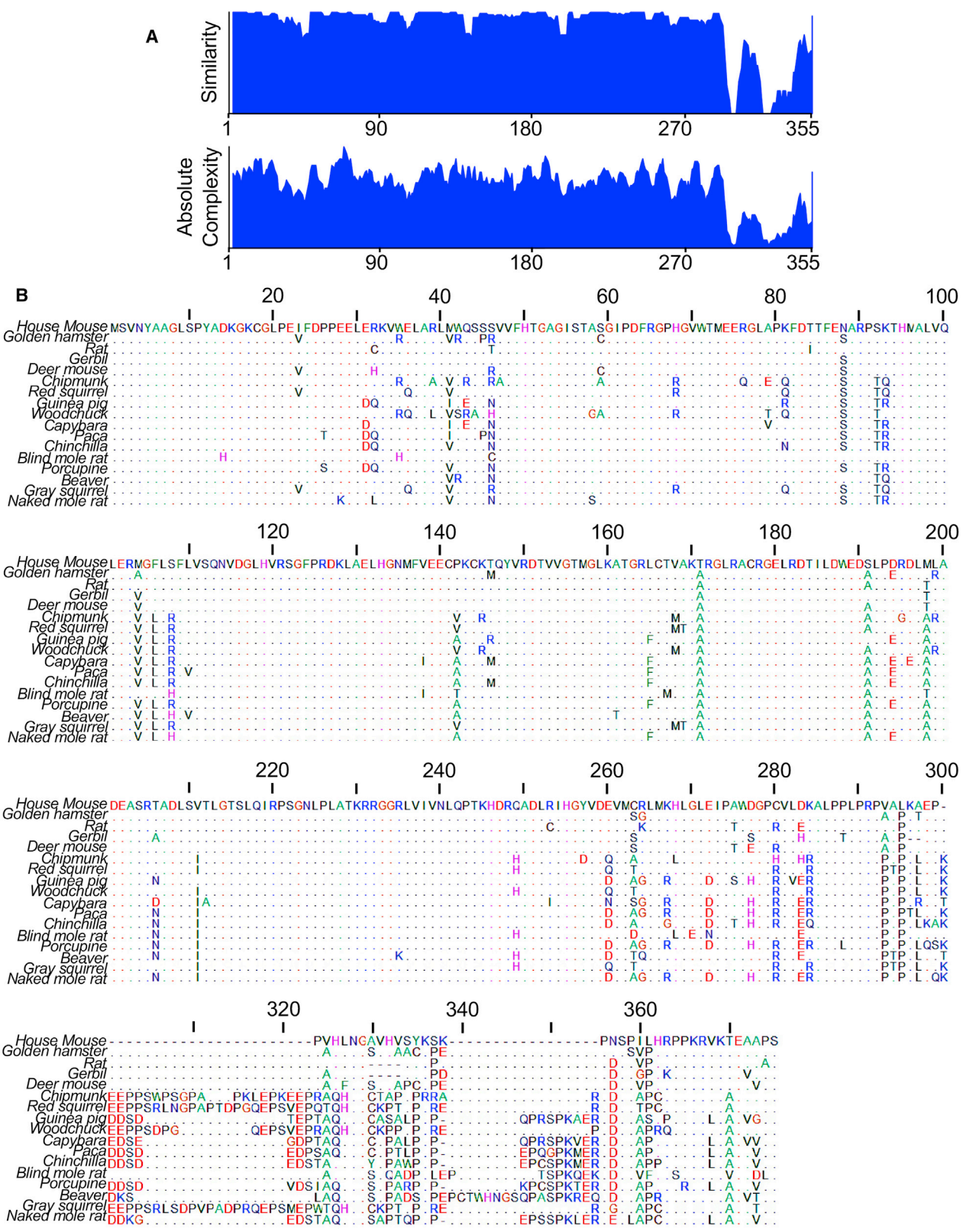

(legend on next page)

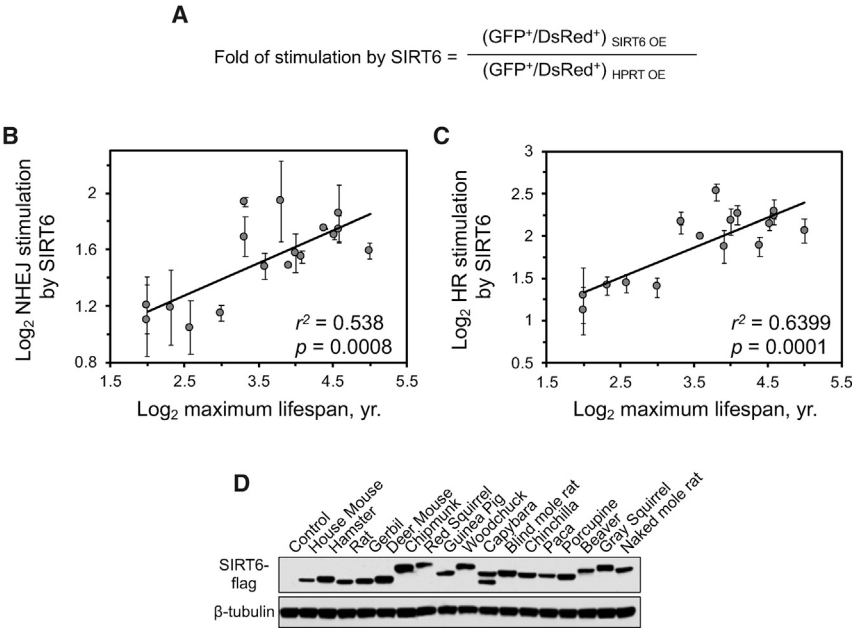

Figure 4. SIRT6 ability to stimulate DSB repair positively correlates with species maximum lifespan

(A) The formula to calculate the fold of DSB repair stimulation by SIRT6. Plasmids overexpressing (OE) HPRT (control) or SIRT6 were co-transfected with the I-SceI and DsRed plasmids, and the fold stimulation for both NHEJ and HR was calculated as shown.

(B) SIRT6 ability to promote NHEJ positively correlates with species maximum lifespan. SIRT6 of rodent species were expressed in mouse fibroblasts containing chromosomally integrated NHEJ reporter cassette (Figure 2A).

(C) SIRT6 ability to promote HR positively correlates with species maximum lifespan. SIRT6 from 18 rodent species were expressed in rat fibroblasts containing chromosomally integrated HR reporter cassette (Figure 2B). All experiments in these figures were repeated at least 3 times and error bars show SD *r*, Pearson correlation coefficient. p values were determined by t test for uncorrected data; the values for phylogenetically corrected data are shown in the main text. Correlation between SIRT6-mediated stimulation of DSB repair and DNA body mass is shown in Figures S5A and S5B.

(D) western blot on the mouse cells expressing flag-tagged SIRT6 cDNAs from the corresponding species, probed with antibodies to flag tag.

lifespan. Subtracting the effect of SIRT6 considerably reduced the correlation coefficient between DSB repair and lifespan (Table S2), indicating that the difference in SIRT6 activity explains a major portion of the correlation between species DSB repair efficiency and MLS.

To further test whether SIRT6 is responsible for more efficient DSB repair in long-lived species, we knocked down SIRT6 in beaver skin fibroblasts that harbor a DSB repair construct and then tested the repair efficiency. Lentivirus-delivered shRNA1 and shRNA2 efficiently reduced the protein level of SIRT6 in beaver cells compared to the mock transduced cells, whereas shRNA3 and shRNA4 were less efficient (Figure S5C). We found that the NHEJ efficiency in the shRNA1 and shRNA2 cells was significantly diminished compared to the mock transduced cells, but not in the shRNA3 or shRNA4 expressing cells (Figure S5D). This result indicates that SIRT6 in long-lived species is required to maintain the high level of DSB repair in beaver cells.

Together, these results indicate that SIRT6 from long-lived species is required to maintain high level of DSB repair in long-lived species and is sufficient to improve DSB repair when expressed in short-lived species.

Five Amino Acids Are Responsible for the Differential Activities of Mouse and Beaver SIRT6 in Stimulating DSB Repair

As the activity of SIRT6 in promoting DNA DSB repair is higher in long-lived rodents, we set out to determine which amino acids (aa) are responsible for the differential SIRT6 activities between short- and long-lived species. We performed analyses on mouse and beaver SIRT6 proteins, as they represent a weak SIRT6 from a short-lived species and a strong SIRT6 from a long-lived species, respectively. We constructed mouse-beaver chimeric proteins starting with the divergent C terminus. Swapping C-termini beginning with P292 between mouse and beaver SIRT6 did not affect their activities (Figure 5A). We next swapped the C-termini starting from G270, which is the last amino acid of the structured region (Pan et al., 2011). The resulting fusion proteins maintained the activity levels determined by the N-terminal portions of the chimeric proteins (Figure 5A), indicating that the C terminus, though relatively more divergent between species (Figures 3A and 3B), is not a critical determinant of interspecies differences in SIRT6 activity.

Next, we swapped a larger portion of the C-termini, starting from R220. Swapping these regions significantly increased the activity of the mouse SIRT6 and reduced the activity of the beaver SIRT6 (Figure 5A). Considering that the C terminus after G270 is not critical in determining SIRT6 activity (Figure 5A), we reasoned that the sequence from aa 221 to aa 270 is critical. Consistent with this notion, when the regions between P221 and G270 were swapped, the mutant mouse SIRT6 increased its activity to the level of the WT beaver SIRT6, and the mutant beaver SIRT6 decreased its activity to the level of the WT mouse SIRT6 (Figure 5B). This result was confirmed in SIRT6 knockout MEF cells (Figure S5E). Thus, we identified the region that was fully

Figure 3. Alignment of Rodent SIRT6 Proteins

(A) Alignment of rodent SIRT6 proteins indicated by amino acid similarity and absolute complexity. The alignment of SIRT6 from 18 rodent species (Figure S1) was performed with AlignX module in Vector NTI software where the blosum62mt2 scoring matrix was used.

(B) Alignment of SIRT6 protein sequences from 18 rodent species. The alignment was performed with ClustalW multiple sequence alignment program. Dots indicate amino acids identical to the mouse sequence. The SIRT6 sequences were placed in the order of increasing maximum lifespan of the species.

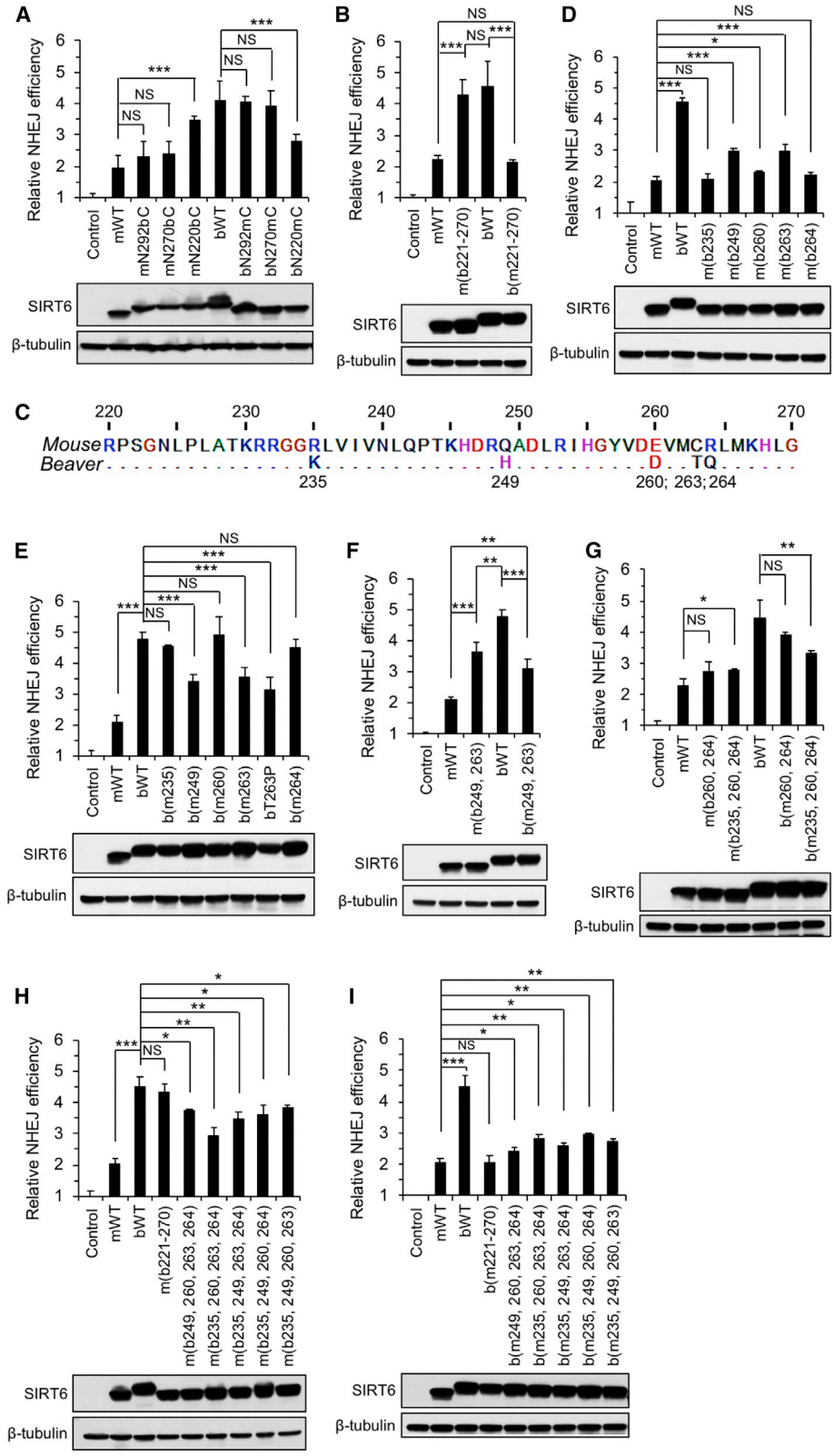

(legend on next page)

responsible for the difference in activity between the mouse and the beaver SIRT6 proteins.

Within the aa 221–270 region, mouse and beaver SIRT6 proteins differ by 5 residues: residues 235, 249, 260, 263, and 264 (Figure 5C). To determine the significance of each residue, we generated single-aa replacements in both mouse and beaver SIRT6 proteins. Though none of these single amino acid mutants completely reversed SIRT6 activity, replacing aa 249 or 263 had a stronger impact on SIRT6 activity than replacing aa 235, 260, or 264, indicated by both mouse SIRT6 mutants (Figure 5D) and beaver SIRT6 mutants (Figure 5E). Interestingly, when a human tumor-associated SIRT6 mutation, T263P (Kugel et al., 2015), was introduced into beaver SIRT6, there also was a significant decrease in SIRT6 activity (Figure 5E). Though aa 249 and aa 263 are individually more important to SIRT6 activity, double mutants that combined both substitutions failed to fully swap the mouse and beaver SIRT6 activities (Figure 5F). Alternatively, though aa 235, 260, and 264 are less important individually, combining the three substitutions in a triple mutant could significantly change SIRT6 activity, especially for the beaver SIRT6 mutant (Figure 5G). Next, quadruple mutants were generated to test whether any four out of the five aa substitutions are sufficient to swap mouse and beaver SIRT6 activities. Though significant changes of SIRT6 activity were achieved with the quadruple replacements, none of them were able to completely reverse the activity of SIRT6 in promoting DSB repair (Figures 5H and 5I), suggesting that all the five amino acids are involved. We also tested the function of these five amino acids using γ-H2AX foci quantification. We found that beaver WT and mouse 5-mut SIRT6 proteins are more efficient in resolving DNA damage induced by 8 Gy of γ-radiation than mouse WT and beaver 5-mut SIRT6 proteins (Figures S5F and S5G). This result confirmed that the identified five aa are critical in determining the difference in SIRT6 activities in DNA repair between mouse and beaver.

Collectively, we conclude that all the five substitutions are necessary and sufficient to explain the difference between mouse and beaver SIRT6 activities. These data also suggest that the corresponding five aa residues in the beaver SIRT6 cooperate in a way to confer the beaver protein a stronger activity in stimulating DSB repair.

The Five aa Substitutions Change Enzymatic Activities between Mouse and Beaver SIRT6

SIRT6 harbors mono-ADP-ribosyltransferase activity (Liszt et al., 2005) and histone deacetylase activity (Michishita et al., 2008). Both enzymatic activities were previously shown to be involved in regulating DSB repair (Mao et al., 2011). Therefore, we tested if the identified five aa differences between the mouse and beaver proteins affect the SIRT6 enzymatic activities.

We purified recombinant mouse WT SIRT6, mouse SIRT6 with five beaver aa replacements (mouse 5mut), beaver WT SIRT6 and beaver SIRT6 with five mouse aa replacements (beaver 5mut). Mouse 5mut and beaver WT SIRT6 proteins showed stronger deacetylase activities on all three known SIRT6 histone targets, H3K9, H3K18, and H3K56 (Figure 6A). Importantly, there were no statistical differences between mouse 5mut and beaver WT, or between mouse WT and beaver 5mut in deacetylation activities (Figure 6A), indicating that the identified five aa residues are fully responsible for the differential deacetylation activities between mouse and beaver SIRT6 proteins. Similarly, mono-ADP-ribosyltransferase activity was higher in the beaver WT and mouse 5mut SIRT6s compared to mouse WT and beaver 5mut SIRT6s (Figure 6B). We previously found that SIRT6 ribosylates PARP1 and activates its poly-ADP-ribosyltransferase activity to promote DSB repair (Mao et al., 2011). Here, we found that beaver WT and mouse 5mut SIRT6s are more robust at stimulating PARP1 activity (Figure 6C). Though beaver WT SIRT6 has a significantly lower melting temperature (Tm) than mouse WT SIRT6, the identified five aa did not change the thermal stability

Figure 5. Five amino acid substitutions are responsible for the differential activities between mouse and beaver SIRT6

Chimeric mouse and beaver SIRT6 proteins were tested for their ability to stimulate NHEJ in mouse fibroblasts containing chromosomally integrated NHEJ reporter construct (Figure 2A). Lower panels show western blots on the mouse cells expressing SIRT6 proteins, probed with an antibody to SIRT6 (Abcam, ab62739). The epitope that the antibody recognizes is the same between mouse and beaver SIRT6 and their mutants. The following nomenclature of the chimeric proteins is used throughout the figure: m corresponds to mouse; b corresponds to beaver. mWT corresponds to mouse WT SIRT6; bWT corresponds to beaver WT SIRT6; mNXbC is a SIRT6 protein with mouse N-terminal portion and beaver C-terminal portion starting from amino acid X; m(bX) is a mouse SIRT6 protein where aa X was replaced with a corresponding beaver amino acid; b(mX, Y) is a beaver SIRT6 protein where amino acids X and Y were replaced with the corresponding mouse amino acids.

(A) Swapping C-terminal regions between mouse and beaver SIRT6.

(B) Swapping amino acid 221-270 region between mouse and beaver SIRT6 is sufficient to fully swap the mouse and beaver SIRT6 activities.

(C) SIRT6 sequence between amino acids 220-270. The differences between mouse and beaver are indicated.

(D) Introducing any single amino acid substitution into the mouse SIRT6 corresponding to the beaver amino acid sequence in the 221-270 region is not sufficient to increase the mouse SIRT6 activity to the level of the beaver SIRT6.

(E) Introducing any single amino acid substitution into the beaver SIRT6 corresponding to the mouse amino acids in 221-270 region is not sufficient to decrease the beaver SIRT6 activity to the level of the mouse SIRT6.

(F) Replacing amino acids 249 and 263 together is not sufficient to swap the mouse and beaver SIRT6 activities.

(G) Replacing amino acids 235, 260, and 264 is not sufficient to swap the mouse and beaver SIRT6 activities.

(H) None of the quadruple amino acid replacements in the mouse SIRT6 elevate its activity to the level of the beaver SIRT6 or to the level of the quintuple replacement that involves the entire 221-270 region m(b221-270).

(I) None of the quadruple amino acid replacements in the beaver SIRT6 reduce its activity to the level of the mouse SIRT6 or to the level of the quintuple replacement that involves the entire 221-270 region b(m221-270).

All experiments were repeated at least three times and error bars show SD Statistical significance was determined using one-way ANOVA with Tukey's post hoc test. NS, not significant; *$p < 0.05$, **$p < 0.01$; ***$p < 0.001$.

See also Figure S5.

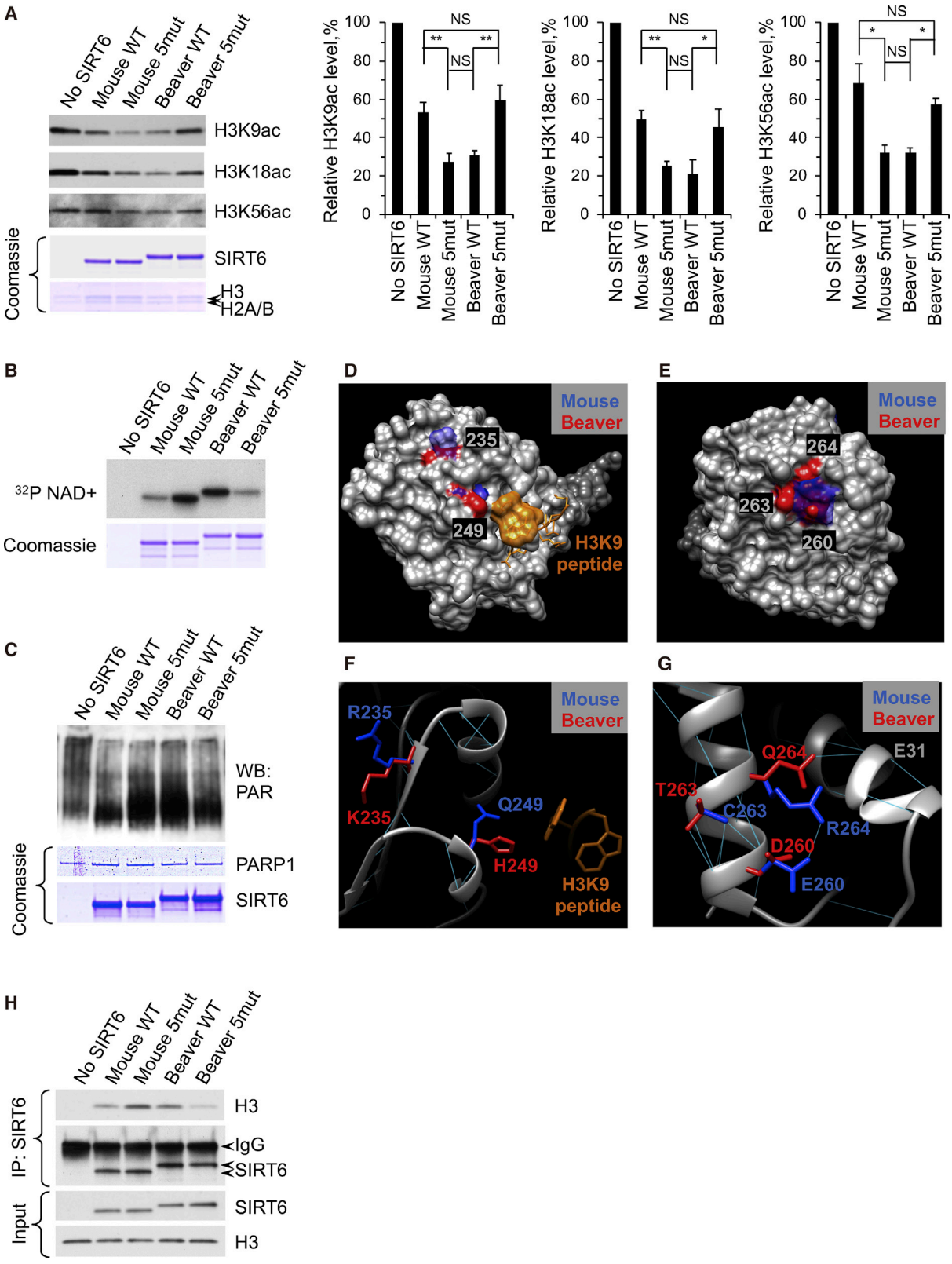

(legend on next page)

of the proteins (Figure S6A). Furthermore, the five aa replacements did not change the protein stability in cells measured by pulse chase assays (Figure S6B). Taken together, these results indicate that the five aa replacements between the mouse and beaver SIRT6 change the enzymatic activities of SIRT6 without affecting protein stability.

Next, to define the location of the five aas, we modeled the mouse and beaver SIRT6 structures based on the crystal structure of the human SIRT6 (Pan et al., 2011). All five aas are located on the surface of the protein in both mouse and beaver SIRT6 structures (Figures 6D and 6E). Residues 235 and 249 are located in the vicinity of the substrate-binding site (Figure 6F), suggesting that the mouse-beaver aa substitutions may alter the affinity to the substrate. Indeed, the beaver WT and mouse 5mut SIRT6s show stronger affinity to the nucleosome *in vitro* (Figure 6H). aa residues 260, 263, and 264 cluster together on the opposite side of the protein (Figure 7G). In the mouse SIRT6, E260 and R264 form a salt bridge, absent in the beaver SIRT6. The absence of this salt bridge may provide greater flexibility to the adjacent helix in the beaver SIRT6 and enhance its enzymatic activity. Collectively, these results suggest that the enzymatic activities of SIRT6 were enhanced during the evolution of longevity. We also provide evidence that this enhanced activity can be fully attributed to the identified five aa residues in the case of beaver SIRT6.

Beaver SIRT6 Has Lower K_m and Higher V_m than Mouse SIRT6

SIRT6 displays relatively weak deacetylase activity (Feldman et al., 2013). Given that SIRT6 activity is greatly increased with longer acyl chains such as myristoyl (MYR), and de-MYR activity employs the same catalytic site as NAD^+ cofactor as deacetylase, we used de-MYR activity as a proxy for all deacetylase and deacylase activities. We determined K_m and V_m for both NAD^+ cofactor and MYR peptide (Figure S6C). Interestingly, we found that the hierarchy of beaver and mouse alleles largely remains intact even in the de-MYR assay. Beaver SIRT6 displayed higher activity compared to mouse SIRT6 and substitution of the five key beaver residues with mouse residues significantly reduced beaver activity. The beaver backbone generally appeared to significantly increase the affinity for the MYR peptide substrate as indicated by the relatively low K_m of both beaver alleles compared to mouse wild-type or mutant. In contrast to beaver wild-type and mutant, mouse wild-type and mutant alleles failed to show a dramatic difference using the de-MYR assay. This may be due to additional factors controlling SIRT6 activity on nucleosomal substrates. Taken together, our data support the idea that beaver SIRT6 alleles are catalytically more robust compared to mouse alleles; yet additional factors may affect relative activities in the case of nucleosomal substrates or *in vivo*.

Beaver SIRT6 Leads to Stronger Decrease in Stress-Induced Senescence and a Longer Lifespan Compared to Mouse SIRT6

We next tested the physiological function of stronger SIRT6. Senescent cells accumulate during aging, which impairs tissue function and contributes to age-related frailty and diseases. Here, we tested if a stronger SIRT6 is better at protecting cells from senescence.

We generated SIRT6 knockout human dermal fibroblasts using CRISPR (Figures S7A–S7C). The confirmed knockout clone was expanded and transduced with lentiviruses encoding GFP, mouse WT, mouse 5mut, beaver WT, or beaver 5mut SIRT6. The lentivirus used for transduction was titrated to achieve similar levels of expression across the four SIRT6 proteins (Figure 7A). Clonogenic assays after serial doses of γ-radiation showed that the cells expressing beaver WT and mouse 5mut SIRT6 were more resistant than the cells expressing mouse WT and beaver 5mut (Figure S7D and Figure 7B), which is consistent with their differential activities in promoting DSB repair. We then performed β-galactosidase (β-gal) staining after 5 Gy or 10 Gy of γ-radiation. Twelve days after 5 Gy of radiation, cells expressing beaver WT and mouse 5mut SIRT6 showed significantly lower percentage of β-gal positive cells than the cells expressing mouse WT and beaver 5mut SIRT6 proteins (Figures 7C and 7D). At 10 Gy, nearly all cells stained β-gal positive (Figure S7E), suggesting that the DNA repair machinery was overwhelmed at this dose.

Next, we tested if a stronger SIRT6 *in vivo* can lead to a longer lifespan. We generated transgenic *Drosophila* lines overexpressing mouse SIRT6, beaver SIRT6, and their corresponding mutants using PhiC31 integrase-based transgenesis system. The transgenes under the control of a GAL4-indicible promoter

Figure 6. The five amino acid changes confer the beaver SIRT6 higher deacetylation and mono-ADP-ribosylation activities relative to the mouse SIRT6

(A) Deacetylation assays with mouse and beaver SIRT6 proteins. Recombinant mouse WT, mouse WT with five beaver substitutions (mouse 5mut), beaver WT, and beaver with five mouse amino acid substitutions (beaver 5mut) SIRT6 were incubated with purified nucleosomes. The acetylation status of SIRT6 targets was assayed with acetyl-specific antibodies. The graphs on the right show quantification. The experiments were repeated 3 times and error bars show SD Statistical significance was determined using one-way ANOVA with Tukey's post hoc test. NS, not significant; *$p < 0.05$, **$p < 0.01$.

(B) Self mono-ADP-ribosylation assays with mouse and beaver SIRT6 proteins.

(C) PARP1 activation assay. SIRT6 proteins were incubated with PARP1, NAD, and linearized DNA. Poly-ADP ribose (PAR) was visualized with PAR-specific antibodies.

(D-E) Structural analysis of the five amino acids in SIRT6. (D) amino acids 235 and 249 and (E) amino acids 260, 263, and 264 localize on the surface of the protein.

(F) A closer view of amino acids 235 and 249. Both amino acids are located in the vicinity of H3K9 myristoyl peptide.

(G) A closer view of amino acids 260, 263, and 264. Interactions of amino acid side chains between amino acids 260 and 264 in the mouse SIRT6 are altered in the beaver SIRT6.

(H) Nucleosome binding by SIRT6. SIRT6 proteins were incubated with purified HeLa nucleosomes, immunoprecipitated with SIRT6 antibodies, and probed with antibodies against H3.

See also Figure S6.

A

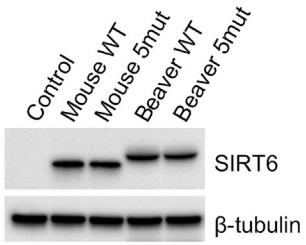

B

Transgene	LD50 (95% CI), Gy	LD75 (95% CI), Gy
Control	0.77 (0.57-0.99)	1.54 (1.24-1.85)
Mouse WT	0.84 (0.68-1.02)	1.68 (1.44-1.93)
Mouse 5mut	1.59 (1.46-1.71)	2.52 (2.35-2.71)
Beaver WT	1.42 (1.22-1.60)	2.40 (2.17-2.68)
Beaver 5mut	0.90 (0.76-1.05)	1.80 (1.60-2.00)

C

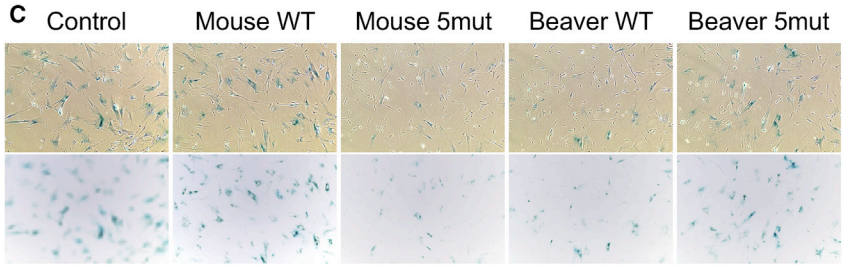

D

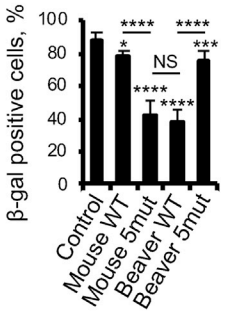

E

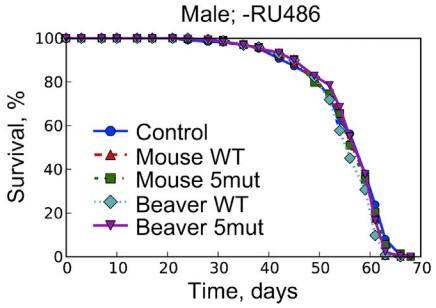

F

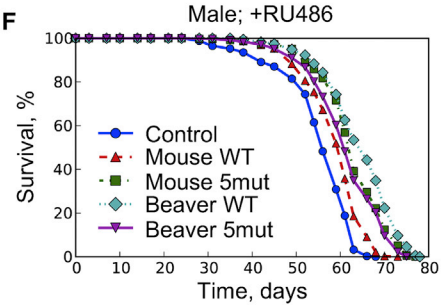

G

Genotypes	RU486	n	Median lifespan (Days)	Change %	Maximum lifespan (Days)	Change %	*p*-value Log Rank	*p*-value Wilcoxon
Control	–	323	57	-	68	-	-	-
Mouse WT	–	361	57	0%	66	-2.9%	0.03	NS
Mouse 5mut	–	351	56	-1.8%	68	0%	NS	NS
Beaver WT	–	348	55	-3.5%	66	-2.9%	4.5×10^{-05}	0.009
Beaver 5mut	–	349	57	0%	68	0%	NS	NS
Control	+	340	56	-	68	-	-	-
Mouse WT	+	366	59	**5.4%**	73	**7.4%**	$<1.0\times10^{-10}$	$<1.0\times10^{-10}$
Mouse 5mut	+	355	62	**10.7%**	77	**13.2%**	$<1.0\times10^{-10}$	$<1.0\times10^{-10}$
Beaver WT	+	350	64	**14.3%**	78	**14.7%**	$<1.0\times10^{-10}$	$<1.0\times10^{-10}$
Beaver 5mut	+	355	61	**8.9%**	75	**10.3%**	$<1.0\times10^{-10}$	$<1.0\times10^{-10}$

H

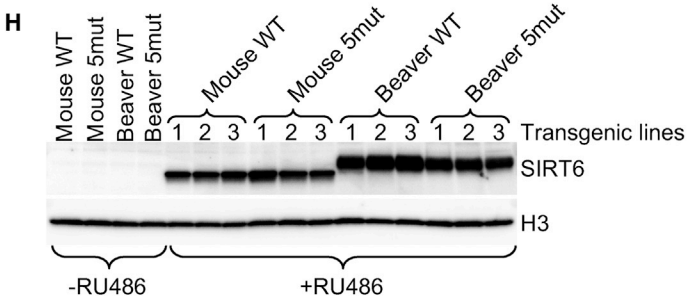

(legend on next page)

were integrated into the same locus on Chromosome 2, 2L(25C6). The transgenic lines were crossed with a RU486-inducible Actin-GeneSwitch strain to achieve ubiquitous expression of SIRT6 upon induction in adulthood. Remarkably, lifespan assays showed that beaver WT and mouse 5mut SIRT6s extended lifespan to a much greater extent than mouse WT SIRT6 in both male (Figures 7E–7G) and female (Figures S7F–S7H) *Drosophila*. Furthermore, beaver 5mut SIRT6 conferred lower lifespan extension compared to beaver WT SIRT6 in both male (Figures 7E–7G) and female (Figures S7F–S7H) flies. These lifespan results followed similar trend with the differential activities of SIRT6 in promoting DSB repair, indicating that stronger SIRT6 leads to a longer lifespan. The lifespan of mouse 5mut expressing lines did not reach the same lifespan as beaver WT expressing lines (Figures 7E–7G), which may be due to the lower expression of mouse 5mut than beaver WT SIRT6 (Figure 7H). However, the mouse 5mut lines lived significantly longer than the mouse WT lines, indicating that the identified five aas affect lifespan when protein expression levels are similar.

Cumulatively, these data suggest that SIRT6 is a key factor responsible for more efficient DSB repair that co-evolved with longevity in long-lived species. Stronger SIRT6 from long-lived species confers longer lifespan than SIRT6 from short-lived species even in a heterologous system.

DISCUSSION

DNA damage has long been implicated in aging. However, the evidence previously reported was based on premature aging phenotypes resulted from increased DNA damage and from defects in DNA repair genes (Hasty et al., 2003). While accelerated aging phenotypes indicate that deficient DNA repair and increased DNA damage are lifespan limiting, this does not necessarily mean that improved DNA repair would be associated with lifespan extension.

Here we report that DNA DSB repair coevolves with longevity. Remarkably, both pathways of DSB repair, HR and NHEJ, are more efficient in long-lived species. Interestingly, NER did not show correlation with MLS. We find that NER efficiency correlates to sun exposure, as the type of damage (bulky DNA adducts) repaired by NER are generated primarily by UV-light, with endogenous sources having only a minor role. Thus, a species' life style (nocturnal or diurnal) imposes stronger selective pressure on NER than the MLS. Therefore, it is possible that, in species with identical levels of sun exposure, NER efficiency would show a correlation to MLS. This caveat likely explains the previously mentioned discrepancy between the earlier studies, with some finding a correlation between NER efficiency and MLS and others not. For example, in the original Hart and Setlow study (Hart and Setlow, 1974), all long-lived species were diurnal (human, elephant, and cow), while all the short-lived species were nocturnal (mouse, rat, and shrew), leading to the observed correlation with MLS.

Why is DSB repair, but not other DNA repair pathways, linked to MLS? NER is correlated more with sun exposure, which makes evolutionary sense, as the primary source of the damage NER repairs comes from UV-light. Additionally, BER, which repairs oxidative damage to DNA, may be too important for everyday function of the cell, allowing little variation in efficiency between species. This could also explain the lack of human syndromes associated with BER deficiency. Another consideration is that both BER and NER pathways repair DNA lesions that primarily result in point mutations. It has been previously shown that point mutations accumulate with age (Stuart and Glickman, 2000), but the rate of accumulation is unlikely to explain age-related decline in tissue function. In contrast, DSBs have much more severe consequences. A single unrepaired DSB can lead to cell cycle arrest or cell death. Mis-repaired DSBs lead to massive rearrangements of genetic material, such as the loss of chromosomal segments and genomic rearrangements. Such events not only change gene sequence, but also change genomic organization by altering higher-order chromatin structure. Epigenetic changes resulting from DNA damage may be important drivers of the aging process by dis-regulating global gene transcription and leading to tissue dysfunction (Gorbunova and Seluanov, 2016; Sen et al., 2016). Therefore, maintaining proper chromatin organization with age becomes critical in long-lived species.

It was recently proposed that DSBs are a driving force of aging via the induction of genomic rearrangements, cellular senescence, and apoptosis (White and Vijg, 2016). Furthermore, DNA DSBs promote redistribution of chromatin-modifying enzymes, leading to accumulation of epigenetic changes and resulting in transcriptional signature similar to that of aged tissues (Oberdoerffer et al., 2008). These observations underscore the importance of DSB repair for longevity. Consistent with our finding, genomic and transcriptomic studies of long-lived animals show that genes involved in DSB repair and DSB signaling

Figure 7. Beaver SIRT6 protects from stress-induced senescence and extends lifespan better than mouse SIRT6

(A) Expression of the mouse, beaver, mouse 5mut, and beaver 5mut SIRT6 proteins in the SIRT6 knockout human dermal fibroblasts.

(B) Clonogenic assay after serial doses of γ-irradiation in cells expressing GFP (control) or SIRT6 proteins. Linear-quadratic model was used to fit the survival data (Figure S7D) and calculate the LD50 and LD75.

(C) Representative images of senescence-associated β-galactosidase (SA β-gal) staining in SIRT6 knockout dermal fibroblasts stably expressing mouse, beaver, or the corresponding mutant SIRT6 proteins after 5 Gy of γ-radiation.

(D) Quantification of SA β-gal positive cells. Images from different areas of the plate were taken and quantified (n = 10). Statistical significance was determined using one-way ANOVA with Tukey's post hoc test. NS, not significant; *p < 0.05, **p < 0.01; ***p < 0.001, ****p < 0.0001.

(E-F) Beaver SIRT6 extends *Drosophila* lifespan better than mouse SIRT6. *Drosophila* transgenic lines expressing mouse WT, mouse 5mut, beaver WT, beaver 5mut SIRT6, and empty vector (EV) control were used to measure lifespan. RU486 was used to induce the expression of SIRT6 proteins. See Figures S7F–S7H for the female results.

(G) Summary of the parameters and statistics of the lifespan measurement. Survival data were analyzed using OASIS 2.

(H) western blot showing expression of the mouse, beaver, and their mutant SIRT6 proteins in *Drosophila* transgenic lines.

See also Figure S7.

are expressed at higher levels than in short-lived species (Ma et al., 2016; MacRae et al., 2015), and/or display the signature of positive selection (de Magalhães and Kean, 2013; Zhang et al., 2013).

Since DSB repair co-evolves with longevity, it is important to find the mechanisms responsible for upregulating DSB repair. This proved to be a challenging task, as the only manipulations previously known to increase the efficiency of either HR or NHEJ was by downregulating one of the pathways. However, our data showed that both pathways are upregulated in long-lived species. Furthermore, previous attempts to increase DSB repair efficiency by overexpressing DSB repair enzymes gave disappointing results, as they often resulted in decreased repair and cellular toxicity. We previously found that overexpression of SIRT6 was the only approach capable of increasing both DSB repair pathways without causing negative effects (Mao et al., 2011).

By comparing the ability of SIRT6 from 18 species of rodents to promote DSB repair in mouse cells, we found that longer-lived species have more efficient SIRT6 proteins. SIRT6 activity showed very strong positive correlation with MLS, albeit it was lower that the correlation between DSB repair and MLS. This indicates that additional adaptations, such as elevated expression or sequence changes in other repair factors, also contribute to more efficient DSB repair in long-lived species.

By using a species pair with highly divergent lifespans (mouse and beaver), we identified five aas fully responsible for the difference in SIRT6 activities between the two species. The five aa replacements affected both enzymatic activities of SIRT6: deacetylation and mono-ADP ribosylation. Beaver SIRT6 was a much stronger deacetylase and mono-ADP ribosylase than the mouse SIRT6. Interestingly, the mono-ADP ribosylation activity seems to show greater difference between mouse and beaver SIRT6s than the deacetylation activity. Since mono-ADP ribosylation has been linked to DNA repair, while deacetylation activity of SIRT6 is implicated in gene regulation (Kugel and Mostoslavsky, 2014), this may suggest that DNA repair function of SIRT6 is influenced by MLS to a greater extent.

It is important to note that the five critical aas we identified in mouse and beaver are specific to this species pair. When all the available SIRT6 sequences are aligned, long-lived species tend to have Histidine in position 249 while short-lived species have Glutamine. Long-lived species also have Threonine in position 263, while short-lived species tend to have Cysteine or Serine. The other three aas do not show a consistent pattern across species with respect to MLS. Thus, if we were to perform mutation analysis of other species pairs, we would expect to find partially overlapping sets of aas conferring higher DNA repair efficiency to long-lived species.

Remarkably, we found that beaver SIRT6 as well as mouse SIRT6 with five beaver substitutions, which has improved DNA repair function, lead to a longer lifespan in *Drosophila* than mouse SIRT6. This indicates that the activity of SIRT6 directly contributes to lifespan extension with more active SIRT6 conferring longer lifespan. Our findings pave the way for designing pharmacological interventions to modulate SIRT6 activity. For example, small molecules may be designed that change SIRT6 conformation to resemble that of the long-lived animals. Such activators may then be used to improve DNA DSB repair and possibly alleviate or delay the onset of multiple age-related diseases.

In conclusion, this work demonstrates that identifying protein features that evolved in long-lived animal species and subsequently engineering them in other organisms is a feasible and promising strategy to push the limits of longevity.

STAR★METHODS

Detailed methods are provided in the online version of this paper and include the following:

- KEY RESOURCES TABLE
- CONTACT FOR REAGENT AND RESOURCE SHARING
- EXPERIMENTAL MODEL AND SUBJECT DETAILS
  - Rodents
  - Drosophila
  - Primary cell cultures
  - Cell lines
- METHOD DETAILS
  - Host cell reactivation assay
  - UV sensitivity assay and calculation of LD50
  - Generation of NHEJ and HR reporter cell lines
  - DSB repair assays and FACS analysis
  - Cloning Sirt6 from rodents and mutagenesis
  - Immunofluorescence and foci quantification
  - CRISPR/Cas9-mediated knockout of SIRT6
  - Construction of lentiviral overexpression vectors
  - Construction of lentiviral miRNA vectors
  - Lentiviral production and transduction
  - Clonogenic assay
  - Senescence-associated β-galactosidase (SA-β-gal) staining
  - Protein purification
  - Histone deacetylation assays
  - ADP-ribosylation assay
  - Thermal denaturation assay
  - SIRT6 de-myristoylation assay
  - Pulse-chase assays
  - Protein structure analysis
  - *In vitro* co-immunoprecipitation assay
  - Fly lines, husbandry, and lifespan assays
- QUANTIFICATION AND STATISTICAL ANALYSIS
  - Phylogenetically independent contrast analysis
  - Phylogenetic ANOVA

SUPPLEMENTAL INFORMATION

Supplemental Information can be found online at https://doi.org/10.1016/j.cell.2019.03.043.

ACKNOWLEDGMENTS

We thank Dr. Daven Presgraves for suggestions on statistical analysis and Nicholas Macoretta for critically reading the manuscript. This work was supported by the US National Institutes of Health grants to V.G., A.S., V.N.G., Z.Z., and J.V.; and Life Extension Foundation to V.G. and A.S.

AUTHOR CONTRIBUTIONS

X.T., A.S., and V.G. designed research, analyzed data, and wrote the manuscript; X.T., D.F., Zhihui Zhang, Y.C., W.D., L.L., G.T., R.T., S.H., J.S., K.Z., M.S., Z.M., A.G., A.W., and K.M. performed experiments; A.J., J.-N.Y., A.C., and B.M. analyzed data; B.K.K., D.B, V.N.G., Zhengdong Zhang, and J.V. designed research and contributed to data analysis; A.S. and V.G. supervised research.

DECLARATION OF INTERESTS

The authors declare no competing interests.

Received: December 24, 2018
Revised: January 22, 2019
Accepted: March 21, 2019
Published: April 18, 2019

SUPPORTING CITATIONS

The following references appear in the Supplemental Information: Bovet, 1984; Bovet and Oertli, 1974; Busch et al., 2000; Clarke, 1983; Gattermann et al., 2008; González Pereyra et al., 2008; Grizzell, 1955; Hayes, 1976; Hicks, 1949; Jiménez, 1996; Latham and Mason, 2004; Link et al., 2012; Lord, 1991; Macdonald, 1981; Meagher et al., 2000; Morris and Kendeigh, 1981; Rado et al., 1993; Randall and Thiessen, 1980; Riccio and Goldman, 2000; Rood, 1972; Snyder, 1982; Steele, 1998; Taylor, 1978; Thompson, 1977; Woods; 1973.

REFERENCES

Batista, L.F., Kaina, B., Meneghini, R., and Menck, C.F. (2009). How DNA lesions are turned into powerful killing structures: insights from UV-induced apoptosis. Mutat. Res. *681*, 197–208.

Biasini, M., Bienert, S., Waterhouse, A., Arnold, K., Studer, G., Schmidt, T., Kiefer, F., Gallo Cassarino, T., Bertoni, M., Bordoli, L., and Schwede, T. (2014). SWISS-MODEL: modelling protein tertiary and quaternary structure using evolutionary information. Nucleic Acids Res. *42*, W252-8.

Bodgi, L., Canet, A., Pujo-Menjouet, L., Lesne, A., Victor, J.M., and Foray, N. (2016). Mathematical models of radiation action on living cells: From the target theory to the modern approaches. A historical and critical review. J. Theor. Biol. *394*, 93–101.

Bovet, J. (1984). Strategies of Homing Behavior in the Red Squirrel, Tamiasciurus-Hudsonicus. Behav. Ecol. Sociobiol. *16*, 81–88.

Bovet, J., and Oertli, E.F. (1974). Free-running circadian activity rhythms in free-living beaver (Castor canadensis). J. Comp. Physiol. A Neuroethol. Sens. Neural Behav. Physiol. *92*, 1–10.

Busch, C., Antinuchi, C.D., del Valle, J.C., Kittlein, M., Malizia, A.I., Vassallo, A.I., and Zenuto, R.R. (2000). Population ecology of subterranean rodents. Life underground: the biology of subterranean rodents, E.A. Lacey, J.L. Patton, and G.N. Cameron, eds. (Chicago, Illinois: University of Chicago Press), pp. 183–226.

Clarke, J. (1983). Moonlight's influence on predator/prey interactions between short-eared owls (Asio flammeus) and deermice (Peromyscus maniculatus). Behav. Ecol. Sociobiol. *13*, 205–209.

de Magalhães, J.P., and Kean, M. (2013). Endless paces of degeneration–applying comparative genomics to study evolution's moulding of longevity. EMBO Rep. *14*, 661–662.

Debacq-Chainiaux, F., Erusalimsky, J.D., Campisi, J., and Toussaint, O. (2009). Protocols to detect senescence-associated beta-galactosidase (SA-betagal) activity, a biomarker of senescent cells in culture and in vivo. Nat. Protoc. *4*, 1798–1806.

Dimri, G.P., Lee, X., Basile, G., Acosta, M., Scott, G., Roskelley, C., Medrano, E.E., Linskens, M., Rubelj, I., Pereira-Smith, O., et al. (1995). A biomarker that identifies senescent human cells in culture and in aging skin in vivo. Proc. Natl. Acad. Sci. USA *92*, 9363–9367.

Dollé, M.E.T., Snyder, W.K., Gossen, J.A., Lohman, P.H.M., and Vijg, J. (2000). Distinct spectra of somatic mutations accumulated with age in mouse heart and small intestine. Proc. Natl. Acad. Sci. USA *97*, 8403–8408.

Fabre, P.H., Hautier, L., Dimitrov, D., and Douzery, E.J. (2012). A glimpse on the pattern of rodent diversification: a phylogenetic approach. BMC Evol. Biol. *12*, 88.

Faghri, S., Tamura, D., Kraemer, K.H., and Digiovanna, J.J. (2008). Trichothiodystrophy: a systematic review of 112 published cases characterises a wide spectrum of clinical manifestations. J. Med. Genet. *45*, 609–621.

Feldman, J.L., Baeza, J., and Denu, J.M. (2013). Activation of the protein deacetylase SIRT6 by long-chain fatty acids and widespread deacylation by mammalian sirtuins. J. Biol. Chem. *288*, 31350–31356.

Felsenstein, J. (1985). Phylogenies and the comparative method. Am. Nat. *125*, 1–15.

Francis, A.A., Lee, W.H., and Regan, J.D. (1981). The relationship of DNA excision repair of ultraviolet-induced lesions to the maximum life span of mammals. Mech. Ageing Dev. *16*, 181–189.

Franken, N.A., Rodermond, H.M., Stap, J., Haveman, J., and van Bree, C. (2006). Clonogenic assay of cells in vitro. Nat. Protoc. *1*, 2315–2319.

Garland, T., Dickerman, A.W., Janis, C.M., and Jones, J.A. (1993). Phylogenetic Analysis of Covariance by Computer-Simulation. Syst. Biol. *42*, 265–292.

Garm, C., Moreno-Villanueva, M., Bürkle, A., Petersen, I., Bohr, V.A., Christensen, K., and Stevnsner, T. (2013). Age and gender effects on DNA strand break repair in peripheral blood mononuclear cells. Aging Cell *12*, 58–66.

Gattermann, R., Johnston, R.E., Yigit, N., Fritzsche, P., Larimer, S., Ozkurt, S., Neumann, K., Song, Z., Colak, E., Johnston, J., and McPhee, M.E. (2008). Golden hamsters are nocturnal in captivity but diurnal in nature. Biol. Lett. *4*, 253–255.

Gentleman, R.C., Carey, V.J., Bates, D.M., Bolstad, B., Dettling, M., Dudoit, S., Ellis, B., Gautier, L., Ge, Y., Gentry, J., et al. (2004). Bioconductor: open software development for computational biology and bioinformatics. Genome Biol. *5*, R80.

Gil, R., Barth, S., Kanfi, Y., and Cohen, H.Y. (2013). SIRT6 exhibits nucleosome-dependent deacetylase activity. Nucleic Acids Res. *41*, 8537–8545.

González Pereyra, M.L., Carvalho, E.C., Tissera, J.L., Keller, K.M., Magnoli, C.E., Rosa, C.A., Dalcero, A.M., and Cavaglieri, L.R. (2008). An outbreak of acute aflatoxicosis on a chinchilla (Chinchilla lanigera) farm in Argentina. J. Vet. Diagn. Invest. *20*, 853–856.

Gorbunova, V., and Seluanov, A. (2016). DNA double strand break repair, aging and the chromatin connection. Mutat. Res. *788*, 2–6.

Gorbunova, V., Seluanov, A., Zhang, Z., Gladyshev, V.N., and Vijg, J. (2014). Comparative genetics of longevity and cancer: insights from long-lived rodents. Nat. Rev. Genet. *15*, 531–540.

Grizzell, R.A., Jr. (1955). A study of the southern woodchuck, Marmota monax monax. Am. Midl. Nat. *53*, 257–293.

Grube, K., and Bürkle, A. (1992). Poly(ADP-ribose) polymerase activity in mononuclear leukocytes of 13 mammalian species correlates with species-specific life span. Proc. Natl. Acad. Sci. USA *89*, 11759–11763.

Han, S.K., Lee, D., Lee, H., Kim, D., Son, H.G., Yang, J.S., Lee, S.V., and Kim, S. (2016). OASIS 2: online application for survival analysis 2 with features for the analysis of maximal lifespan and healthspan in aging research. Oncotarget *7*, 56147–56152.

Harper, J.M., Salmon, A.B., Leiser, S.F., Galecki, A.T., and Miller, R.A. (2007). Skin-derived fibroblasts from long-lived species are resistant to some, but not all, lethal stresses and to the mitochondrial inhibitor rotenone. Aging Cell *6*, 1–13.

Hart, R.W., and Setlow, R.B. (1974). Correlation between deoxyribonucleic acid excision-repair and life-span in a number of mammalian species. Proc. Natl. Acad. Sci. USA *71*, 2169–2173.

Hasty, P., Campisi, J., Hoeijmakers, J., van Steeg, H., and Vijg, J. (2003). Aging and genome maintenance: lessons from the mouse? Science *299*, 1355–1359.

Hayes, S.R. (1976). Daily activity and body temperature of the southern woodchuck, Marmota monax monax, in northwestern Arkansas. J. Mammal. *57*, 291–299.

Hicks, E.A. (1949). Ecological factors affecting the activity of the western fox squirrel, Sciurus niger rufiventer (Geoffroy). Ecol. Monogr. *19*, 287–302.

Jiménez, J.E. (1996). The extirpation and current status of wild chinchillas Chinchilla lanigera and C. brevicaudata. Biol. Conserv. *77*, 1–6.

Kanfi, Y., Naiman, S., Amir, G., Peshti, V., Zinman, G., Nahum, L., Bar-Joseph, Z., and Cohen, H.Y. (2012). The sirtuin SIRT6 regulates lifespan in male mice. Nature *483*, 218–221.

Kapahi, P., Boulton, M.E., and Kirkwood, T.B. (1999). Positive correlation between mammalian life span and cellular resistance to stress. Free Radic. Biol. Med. *26*, 495–500.

Karikkineth, A.C., Scheibye-Knudsen, M., Fivenson, E., Croteau, D.L., and Bohr, V.A. (2017). Cockayne syndrome: Clinical features, model systems and pathways. Ageing Res. Rev. *33*, 3–17.

Kato, H., Harada, M., Tsuchiya, K., and Moriwaki, K. (1980). Absence of Correlation between DNA-Repair in Ultraviolet Irradiated Mammalian-Cells and Life-Span of the Donor Species. Jpn. J. Genet. *55*, 99–108.

Kugel, S., and Mostoslavsky, R. (2014). Chromatin and beyond: the multitasking roles for SIRT6. Trends Biochem. Sci. *39*, 72–81.

Kugel, S., Feldman, J.L., Klein, M.A., Silberman, D.M., Sebastián, C., Mermel, C., Dobersch, S., Clark, A.R., Getz, G., Denu, J.M., and Mostoslavsky, R. (2015). Identification of and Molecular Basis for SIRT6 Loss-of-Function Point Mutations in Cancer. Cell Rep. *13*, 479–488.

Lapytsko, A., Kollarovic, G., Ivanova, L., Studencka, M., and Schaber, J. (2015). FoCo: a simple and robust quantification algorithm of nuclear foci. BMC Bioinformatics *16*, 392.

Latham, N., and Mason, G. (2004). From house mouse to mouse house: the behavioural biology of free-living Mus musculus and its implications in the laboratory. Appl. Anim. Behav. Sci. *86*, 261–289.

Link, A., Di Fiore, A., Galvis, N., and Fleming, E. (2012). Patterns of mineral lick visitation by lowland tapir (Tapirus terrestris) and lowland paca (Cuniculus paca) in a western amazonian rainforest in Ecuador. Mastozool. Neotrop. *19*.

Liszt, G., Ford, E., Kurtev, M., and Guarente, L. (2005). Mouse Sir2 homolog SIRT6 is a nuclear ADP-ribosyltransferase. J. Biol. Chem. *280*, 21313–21320.

Lord, R.D. (1991). 24-Hour Activity and Coprophagy by Capybaras (Hydrochaeris-Hydrochaeris). Stud. Neotrop. Fauna Environ. *26*, 113–120.

Lorenzini, A., Johnson, F.B., Oliver, A., Tresini, M., Smith, J.S., Hdeib, M., Sell, C., Cristofalo, V.J., and Stamato, T.D. (2009). Significant correlation of species longevity with DNA double strand break recognition but not with telomere length. Mech. Ageing Dev. *130*, 784–792.

Ma, S., Upneja, A., Galecki, A., Tsai, Y.M., Burant, C.F., Raskind, S., Zhang, Q., Zhang, Z.D., Seluanov, A., Gorbunova, V., et al. (2016). Cell culture-based profiling across mammals reveals DNA repair and metabolism as determinants of species longevity. eLife *5*.. https://doi.org/10.7554/eLife.19130.

Macdonald, D. (1981). Dwindling resources and the social behaviour of capybaras,(Hydrochoerus hydrochaeris)(Mammalia). J. Zool. *194*, 371–391.

MacRae, S.L., Croken, M.M., Calder, R.B., Aliper, A., Milholland, B., White, R.R., Zhavoronkov, A., Gladyshev, V.N., Seluanov, A., Gorbunova, V., et al. (2015). DNA repair in species with extreme lifespan differences. Aging (Albany NY) *7*, 1171–1184.

Mao, Z., Hine, C., Tian, X., Van Meter, M., Au, M., Vaidya, A., Seluanov, A., and Gorbunova, V. (2011). SIRT6 promotes DNA repair under stress by activating PARP1. Science *332*, 1443–1446.

Meagher, S., Penn, D.J., and Potts, W.K. (2000). Male-male competition magnifies inbreeding depression in wild house mice. Proc. Natl. Acad. Sci. USA *97*, 3324–3329.

Meredith, R.W., Janečka, J.E., Gatesy, J., Ryder, O.A., Fisher, C.A., Teeling, E.C., Goodbla, A., Eizirik, E., Simão, T.L., Stadler, T., et al. (2011). Impacts of the Cretaceous Terrestrial Revolution and KPg extinction on mammal diversification. Science *334*, 521–524.

Michishita, E., McCord, R.A., Berber, E., Kioi, M., Padilla-Nash, H., Damian, M., Cheung, P., Kusumoto, R., Kawahara, T.L., Barrett, J.C., et al. (2008). SIRT6 is a histone H3 lysine 9 deacetylase that modulates telomeric chromatin. Nature *452*, 492–496.

Morris, J.G., and Kendeigh, S.C. (1981). Energetics of the Prairie Deer Mouse Peromyscus maniculatus bairdii. Am. Midl. Nat. *105*, 368–376.

Mostoslavsky, R., Chua, K.F., Lombard, D.B., Pang, W.W., Fischer, M.R., Gellon, L., Liu, P., Mostoslavsky, G., Franco, S., Murphy, M.M., et al. (2006). Genomic instability and aging-like phenotype in the absence of mammalian SIRT6. Cell *124*, 315–329.

Niedernhofer, L.J., Garinis, G.A., Raams, A., Lalai, A.S., Robinson, A.R., Appeldoorn, E., Odijk, H., Oostendorp, R., Ahmad, A., van Leeuwen, W., et al. (2006). A new progeroid syndrome reveals that genotoxic stress suppresses the somatotroph axis. Nature *444*, 1038–1043.

Oberdoerffer, P., Michan, S., McVay, M., Mostoslavsky, R., Vann, J., Park, S.K., Hartlerode, A., Stegmuller, J., Hafner, A., Loerch, P., et al. (2008). SIRT1 redistribution on chromatin promotes genomic stability but alters gene expression during aging. Cell *135*, 907–918.

Oshima, J., Sidorova, J.M., and Monnat, R.J., Jr. (2017). Werner syndrome: Clinical features, pathogenesis and potential therapeutic interventions. Ageing Res. Rev. *33*, 105–114.

Osterwalder, T., Yoon, K.S., White, B.H., and Keshishian, H. (2001). A conditional tissue-specific transgene expression system using inducible GAL4. Proc. Natl. Acad. Sci. USA *98*, 12596–12601.

Pan, P.W., Feldman, J.L., Devries, M.K., Dong, A., Edwards, A.M., and Denu, J.M. (2011). Structure and biochemical functions of SIRT6. J. Biol. Chem. *286*, 14575–14587.

Paradis, E., Claude, J., and Strimmer, K. (2004). APE: Analyses of Phylogenetics and Evolution in R language. Bioinformatics *20*, 289–290.

Pettersen, E.F., Goddard, T.D., Huang, C.C., Couch, G.S., Greenblatt, D.M., Meng, E.C., and Ferrin, T.E. (2004). UCSF Chimera–a visualization system for exploratory research and analysis. J. Comput. Chem. *25*, 1605–1612.

Promislow, D.E. (1994). DNA repair and the evolution of longevity: a critical analysis. J. Theor. Biol. *170*, 291–300.

Rado, R., Shanas, U., Zuri, I., and Terkel, J. (1993). Seasonal activity in the blind mole rat (Spalax ehrenbergi). Can. J. Zool. *71*, 1733–1737.

Randall, J.A., and Thiessen, D.D. (1980). Seasonal Activity and Thermoregulation in Meriones-Unguiculatus - a Gerbils Choice. Behav. Ecol. Sociobiol. *7*, 267–272.

Revell, L.J. (2012). phytools: an R package for phylogenetic comparative biology (and other things). Methods Ecol. Evol. *3*, 217–223.

Riccio, A.P., and Goldman, B.D. (2000). Circadian rhythms of locomotor activity in naked mole-rats (Heterocephalus glaber). Physiol. Behav. *71*, 1–13.

Rood, J. (1972). Ecological and behavioural comparisons of three genera of Argentine cavies (Animal Behaviour Monographs).

Schuster, S., Roessler, C., Meleshin, M., Zimmermann, P., Simic, Z., Kambach, C., Schiene-Fischer, C., Steegborn, C., Hottiger, M.O., and Schutkowski, M. (2016). A continuous sirtuin activity assay without any coupling to enzymatic or chemical reactions. Sci. Rep. *6*, 22643.

Seluanov, A., Chen, Z., Hine, C., Sasahara, T.H., Ribeiro, A.A., Catania, K.C., Presgraves, D.C., and Gorbunova, V. (2007). Telomerase activity coevolves with body mass not lifespan. Aging Cell *6*, 45–52.

Seluanov, A., Hine, C., Bozzella, M., Hall, A., Sasahara, T.H., Ribeiro, A.A., Catania, K.C., Presgraves, D.C., and Gorbunova, V. (2008). Distinct tumor suppressor mechanisms evolve in rodent species that differ in size and lifespan. Aging Cell *7*, 813–823.

Seluanov, A., Mao, Z., and Gorbunova, V. (2010a). Analysis of DNA double-strand break (DSB) repair in mammalian cells. J. Vis. Exp. *43*. https://doi.org/10.3791/2002.

Seluanov, A., Vaidya, A., and Gorbunova, V. (2010b). Establishing primary adult fibroblast cultures from rodents. J. Vis. Exp. *44*. https://doi.org/10.3791/2033.

Sen, P., Shah, P.P., Nativio, R., and Berger, S.L. (2016). Epigenetic Mechanisms of Longevity and Aging. Cell *166*, 822–839.

Shiloh, Y., and Lederman, H.M. (2017). Ataxia-telangiectasia (A-T): An emerging dimension of premature ageing. Ageing Res. Rev. *33*, 76–88.

Snyder, D.P. (1982). Tamias striatus. Mamm. Species *168*, 1–8.

Steele, M.A. (1998). Tamiasciurus hudsonicus. Mamm. Species *586*, 1–9.

Stuart, G.R., and Glickman, B.W. (2000). Through a glass, darkly: reflections of mutation from *lacI* transgenic mice. Genetics *155*, 1359–1367.

Sykiotis, G.P., and Bohmann, D. (2008). Keap1/Nrf2 signaling regulates oxidative stress tolerance and lifespan in Drosophila. Dev. Cell *14*, 76–85.

Tacutu, R., Craig, T., Budovsky, A., Wuttke, D., Lehmann, G., Taranukha, D., Costa, J., Fraifeld, V.E., and de Magalhães, J.P. (2013). Human Ageing Genomic Resources: integrated databases and tools for the biology and genetics of ageing. Nucleic Acids Res. *41*, D1027–D1033.

Taylor, K.D. (1978). Range of Movement and Activity of Common Rats (Rattus norvegicus) on Agricultural Land. J. Appl. Ecol. *15*, 663–677.

Thompson, D.C. (1977). Diurnal and seasonal activity of the grey squirrel (Sciurus carolinensis). Can. J. Zool. *55*, 1185–1189.

Tian, X., Doerig, K., Park, R., Can Ran Qin, A., Hwang, C., Neary, A., Gilbert, M., Seluanov, A., and Gorbunova, V. (2018). Evolution of telomere maintenance and tumour suppressor mechanisms across mammals. Philos. Trans. R. Soc. Lond. B Biol. Sci. *373*. https://doi.org/10.1098/rstb.2016.0443.

Toiber, D., Erdel, F., Bouazoune, K., Silberman, D.M., Zhong, L., Mulligan, P., Sebastian, C., Cosentino, C., Martinez-Pastor, B., Giacosa, S., et al. (2013). SIRT6 recruits SNF2H to DNA break sites, preventing genomic instability through chromatin remodeling. Mol. Cell *51*, 454–468.

Vaidya, A., Mao, Z., Tian, X., Spencer, B., Seluanov, A., and Gorbunova, V. (2014). Knock-in reporter mice demonstrate that DNA repair by non-homologous end joining declines with age. PLoS Genet. *10*, e1004511.

Vermeij, W.P., Hoeijmakers, J.H.J., and Pothof, J. (2016). Genome Integrity in Aging: Human Syndromes, Mouse Models, and Therapeutic Options. Annu. Rev. Pharmacol. Toxicol. *56*, 427–445.

White, R.R., and Vijg, J. (2016). Do DNA Double-Strand Breaks Drive Aging? Mol. Cell *63*, 729–738.

Woods, C.A. (1973). Erethizon dorsatum. Mamm. Species *29*, 1–6.

Zhang, G., Cowled, C., Shi, Z., Huang, Z., Bishop-Lilly, K.A., Fang, X., Wynne, J.W., Xiong, Z., Baker, M.L., Zhao, W., et al. (2013). Comparative analysis of bat genomes provides insight into the evolution of flight and immunity. Science *339*, 456–460.

STAR★METHODS

KEY RESOURCES TABLE

REAGENT or RESOURCE	SOURCE	IDENTIFIER
Antibodies		
Anti-H3K9ac	Cell Signaling Technology	Cat#9649
Anti-H3K18ac	Abcam	Cat#ab1191
Anti-H3K56ac	Abcam	Cat#ab76307
Anti-H3	Abcam	Cat#ab1791
Anti-PADPR	Abcam	Cat#ab14459
Anti-FLAG	Sigma-Aldrich	Cat#F3165
Anti-beta Tubulin	Abcam	Cat#ab6046
Anti-γH2AX	Millipore	Cat#05-636
Anti-53BP1	Abcam	Cat#ab172580
Anti-γH2AX	Abcam	Cat#ab11174
Anti-SIRT6	Abcam	Cat#ab62739
Goat anti-mouse IgG HRP	Abcam	Cat#ab97023
Goat anti-rabbit IgG HRP	Abcam	Cat#ab6721
Alexa Fluor 488 Goat anti-mouse IgG (H+L)	Thermo Fisher	Cat#A28175
Alexa Fluor 568 Goat anti-rabbit IgG (H+L)	Thermo Fisher	Cat#A-11011
Bacterial and Virus Strains		
MAX Efficiency Stbl2 competent cells	Thermo Fisher	Cat#10268019
One Shot Stbl3 chemically competent *E. coli*	Thermo Fisher	Cat#C737303
Rosetta-gami B(DE3)pLysS competent cells	Novagen	Cat#71137-4
Chemicals, Peptides, and Recombinant Proteins		
Eagle's Minimum Essential Medium (EMEM)	ATCC	Cat#30-2003
Fetal Bovine Serum (FBS)	Thermo Fisher	Cat#10437028
Penicillin-streptomycin	Thermo Fisher	Cat#15140122
Phosphate-Buffered Saline (PBS)	Corning	Cat#21-040-CV
QIAEX II gel extraction kit	QIAGEN	Cat#20021
Human dermal fibroblast nucleofector kit	Lonza	Cat#VPD-1001
WST-1	Roche	Cat#05015944001
G418, Geneticin	Thermo Fisher	Cat#11811023
Puromycin	Thermo Fisher	Cat#A1113803
Hygromycin	Thermo Fisher	Cat#10687010
Antifade mounting medium with DAPI	Vector laboratories	Cat#H-1200
Polybrene Infection / Transfection Reagent	Millipore	Cat#TR-1003-G
Crystal violet	JT Baker	Cat#F906-03
X-Gal	Thermo Fisher	Cat#15520018
Blocking reagent	Roche	Cat#11096176001
Ni-NTA Agarose	Thermo Fisher	Cat#R90115
HeLa polynucleosomes	EpiCypher	Cat#16-0003
β-Nicotinamide adenine dinucleotide (NAD)	Sigma Aldrich	Cat#N0632-5G
^{32}P NAD+	PerkinElmer	Cat#NEG023X250UC
Protein: PARP1	Sigma Aldrich	Cat#P0996-1KU
Myristoylated TNF-α peptide	GeneScript	Custom peptide
Fish sperm DNA	Thermo Fisher	Cat#15632011
SYPRO orange	Thermo Fisher	Cat#S6650

(*Continued on next page*)

Continued

REAGENT or RESOURCE	SOURCE	IDENTIFIER
EasyTag EXPRESS^{35}S protein labeling mix	PerkinElmer	Cat#NEG772007MC
Dialyzed FBS	Thermo Fisher	Cat#A3382001
HEPES	Thermo Fisher	Cat#15630080
Protease inhibitor cocktail	Roche	Cat#04693132001
Pierce protein A/G agarose	Thermo Fisher	Cat#20421
2x Laemmli sample buffer	Bio-Rad	Cat#1610737
RU486 (mifepristone)	Cayman Chemical	Cat#10006317
Pierce protease inhibitor tablets	Thermo Fisher	Cat#A32965
PhosSTOP	Roche	Cat#4906845001
4x Laemmli sample buffer	Bio-Rad	Cat#1610747
Critical Commercial Assays		
Dual-Luciferase Reporter Assay System	Promega	Cat#E1980
Click-iT Plus EdU Alexa Fluor 647 Imaging Kit	Thermo Fisher	Cat#C10640
Deposited Data		
Beaver Sirt6 CDS	This paper	GenBank: MK482069
Blind mole-rat Sirt6 CDS	This paper	GenBank: MK482070
Capybara Sirt6 CDS	This paper	GenBank: MK482071
Chinchilla Sirt6 CDS	This paper	GenBank: MK482072
Eastern chipmunk Sirt6 CDS	This paper	GenBank: MK482073
Deer mouse Sirt6 CDS	This paper	GenBank: MK482074
Mongolian gerbil Sirt6 CDS	This paper	GenBank: MK482075
Golden hamster Sirt6 CDS	This paper	GenBank: MK482076
Gray squirrel Sirt6 CDS	This paper	GenBank: MK482077
Guinea pig Sirt6 CDS	This paper	GenBank: MK482078
Naked mole-rat Sirt6 CDS	This paper	GenBank: MK482079
Paca Sirt6 CDS	This paper	GenBank: MK482080
Porcupine Sirt6 CDS	This paper	GenBank: MK482081
Red squirrel Sirt6 CDS	This paper	GenBank: MK482082
Woodchuck Sirt6 CDS	This paper	GenBank: MK482083
Experimental Models: Cell Lines		
HEK293T/17	ATCC	Cat#CRL-11268
Human dermal fibroblasts	This paper	N/A
Experimental Models: Organisms/Strains		
D. melanogaster: y^{1} w^{67}c^{23}; P{CaryP}attP40	BestGene	BestGene attP40
D. melanogaster: Actin-GeneSwitch-Gal4	Osterwalder et al., 2001	Gift from Dr. Benoit Biteau, University of Rochester Medical Center
Oligonucleotides		
gRNA to knockout human *SIRT6*	This paper	Table S3
shRNA to knockdown beaver *Sirt6*	This paper	Table S4
Primers for mutagenesis and plasmid construction	This paper	Table S5
Recombinant DNA		
pCMV-Luc	This paper	N/A
pRL-CMV	Promega	Cat#E2261
NHEJ reporter construct	This paper	N/A
HR reporter construct	This paper	N/A
pCMV-Isce1	Mao et al., 2011	Gorbunova lab
pDsRed	Mao et al., 2011	Gorbunova lab

(*Continued on next page*)

Continued

REAGENT or RESOURCE	SOURCE	IDENTIFIER
pEGFP-N1	Clontech	Cat#6085-1
pCMV-mouse Sirt6	This paper	N/A
pCMV-hamster Sirt6	This paper	N/A
pCMV-rat Sirt6	This paper	N/A
pCMV-gerbil Sirt6	This paper	N/A
pCMV-deer mouse Sirt6	This paper	N/A
pCMV-chipmunk Sirt6	This paper	N/A
pCMV-red squirrel Sirt6	This paper	N/A
pCMV-guinea pig Sirt6	This paper	N/A
pCMV-woodchuck Sirt6	This paper	N/A
pCMV-capybara Sirt6	This paper	N/A
pCMV-paca Sirt6	This paper	N/A
pCMV-chinchilla Sirt6	This paper	N/A
pCMV-blind mole rat Sirt6	This paper	N/A
pCMV-porcupine Sirt6	This paper	N/A
pCMV-beaver Sirt6	This paper	N/A
pCMV-gray squirrel Sirt6	This paper	N/A
pCMV-naked mole rat Sirt6	This paper	N/A
pCMV-Flag-mouse Sirt6	This paper	N/A
pCMV-Flag-hamster Sirt6	This paper	N/A
pCMV-Flag-rat Sirt6	This paper	N/A
pCMV-Flag-gerbil Sirt6	This paper	N/A
pCMV-Flag-deer mouse Sirt6	This paper	N/A
pCMV-Flag-chipmunk Sirt6	This paper	N/A
pCMV-Flag-red squirrel Sirt6	This paper	N/A
pCMV-Flag-guinea pig Sirt6	This paper	N/A
pCMV-Flag-woodchuck Sirt6	This paper	N/A
pCMV-Flag-capybara Sirt6	This paper	N/A
pCMV-Flag-paca Sirt6	This paper	N/A
pCMV-Flag-chinchilla Sirt6	This paper	N/A
pCMV-Flag-blind mole rat Sirt6	This paper	N/A
pCMV-Flag-porcupine Sirt6	This paper	N/A
pCMV-Flag-beaver Sirt6	This paper	N/A
pCMV-Flag-gray squirrel Sirt6	This paper	N/A
pCMV-Flag-naked mole rat Sirt6	This paper	N/A
pCMV-mN292bC Sirt6	This paper	N/A
pCMV-mN270bC Sirt6	This paper	N/A
pCMV-mN220bC Sirt6	This paper	N/A
pCMV-bN292mC Sirt6	This paper	N/A
pCMV-bN270mC Sirt6	This paper	N/A
pCMV-bN220mC Sirt6	This paper	N/A
pCMV-m(b221-270) Sirt6	This paper	N/A
pCMV-b(m221-270) Sirt6	This paper	N/A
pCMV-m(b235) Sirt6	This paper	N/A
pCMV-m(b249) Sirt6	This paper	N/A
pCMV-m(b260) Sirt6	This paper	N/A
pCMV-m(b263) Sirt6	This paper	N/A
pCMV-m(b264) Sirt6	This paper	N/A

(*Continued on next page*)

Continued

REAGENT or RESOURCE	SOURCE	IDENTIFIER
pCMV-b(m235) Sirt6	This paper	N/A
pCMV-b(m249) Sirt6	This paper	N/A
pCMV-b(m260) Sirt6	This paper	N/A
pCMV-b(m263) Sirt6	This paper	N/A
pCMV-b(m264) Sirt6	This paper	N/A
pCMV-bT263P Sirt6	This paper	N/A
pCMV-m(b249, 263) Sirt6	This paper	N/A
pCMV-b(m249, 263) Sirt6	This paper	N/A
pCMV-m(b260, 264) Sirt6	This paper	N/A
pCMV-m(b235, 260, 264) Sirt6	This paper	N/A
pCMV-b(m260, 264) Sirt6	This paper	N/A
pCMV-b(m235, 260, 264) Sirt6	This paper	N/A
pCMV-m(b249, 260, 263, 264) Sirt6	This paper	N/A
pCMV-m(b235, 260, 263, 264) Sirt6	This paper	N/A
pCMV-m(b235, 249, 263, 264) Sirt6	This paper	N/A
pCMV-m(b235, 249, 260, 264) Sirt6	This paper	N/A
pCMV-m(b235, 249, 260, 263) Sirt6	This paper	N/A
pCMV-b(m249, 260, 263, 264) Sirt6	This paper	N/A
pCMV-b(m235, 260, 263, 264) Sirt6	This paper	N/A
pCMV-b(m235, 249, 263, 264) Sirt6	This paper	N/A
pCMV-b(m235, 249, 260, 264) Sirt6	This paper	N/A
pCMV-b(m235, 249, 260, 263) Sirt6	This paper	N/A
pSpCas9(BB)-2A-Puro (PX459)	Gift from Dr. Feng Zhang	Addgene Plasmid #62988
PX459-hSIRT6 gRNA1	This paper	N/A
PX459-hSIRT6 gRNA2	This paper	N/A
pLJM1-EGFP	Gift from Dr. David Sabatini	Addgene Plasmid #19319
pLJM1-mouse Sirt6	This paper	N/A
pLJM1-mouse 5mut Sirt6	This paper	N/A
pLJM1-beaver Sirt6	This paper	N/A
pLJM1-beaver 5mut Sirt6	This paper	N/A
pLKO.1 hygro	Gift from Dr. Bob Weinberg	Addgene Plasmid #24150
pLKO.1-hygro-Beaver Sirt6 shRNA-1	This paper	N/A
pLKO.1-hygro-Beaver Sirt6 shRNA-2	This paper	N/A
pLKO.1-hygro-Beaver Sirt6 shRNA-3	This paper	N/A
pLKO.1-hygro-Beaver Sirt6 shRNA-4	This paper	N/A
pET-11a	Novagen	Cat#69436
pET-11a-mouse Sirt6	This paper	N/A
pET-11a-mouse 5mut Sirt6	This paper	N/A
pET-11a-beaver Sirt6	This paper	N/A
pET-11a-beaver 5mut Sirt6	This paper	N/A
pUAST-attB	Sykiotis and Bohmann, 2008	Bohmann lab
pUAST-attB-mouse Sirt6	This paper	N/A
pUAST-attB-mouse 5mut Sirt6	This paper	N/A
pUAST-attB-beaver Sirt6	This paper	N/A
pUAST-attB-beaver 5mut Sirt6	This paper	N/A
Software and Algorithms		
FoCo	Lapytsko et al., 2015	https://sourceforge.net/projects/focicount
FCS Express 6	De Novo Software	www.denovosoftware.com

(*Continued on next page*)

Continued

REAGENT or RESOURCE	SOURCE	IDENTIFIER
sgRNA Scorer 2.0	N/A	https://crispr.med.harvard.edu
Genetic Perturbation Platform	Broad Institute	https://portals.broadinstitute.org/gpp/public
BLOCK-iT RNAi Designer	Thermo Fisher	https://rnaidesigner.thermofisher.com/rnaiexpress
Graphpad Prism 7	GraphPad Software	https://www.graphpad.com/scientific-software/prism
Kaleidagraph	Synergy Software	http://www.synergy.com
SWISS-MODEL	Biasini et al., 2014	https://swissmodel.expasy.org
UCSF Chimera	Pettersen et al., 2004	https://www.cgl.ucsf.edu/chimera
OASIS 2	Han et al., 2016	https://sbi.postech.ac.kr/oasis2
Mesquite	Garland et al., 1993	https://www.mesquiteproject.org
R version 3.2.3	The R Project	https://cran.r-project.org
Other		
BD FACSCanto II Analyzer	BD Biosciences	http://www.bdbiosciences.com
BD LSR II	BD Biosciences	http://www.bdbiosciences.com
Leica TCS SP5 Confocal system	Leica	www.leica-microsystems.com
CFX Connect Real-Time PCR Detection System	Bio-Rad	http://www.bio-rad.com
QuikChange II Site-Directed Mutagenesis Kit	Agilent	Cat#200523
Lenti-X Packaging Single Shots (VSV-G)	Takara	Cat#631275

CONTACT FOR REAGENT AND RESOURCE SHARING

Further information and requests for resources and reagents should be directed to and will be fulfilled by the Lead Contact, Vera Gorbunova (vera.gorbunova@rochester.edu).

EXPERIMENTAL MODEL AND SUBJECT DETAILS

Rodents

All experiments were performed according to procedures approved by the University of Rochester Committee on Animal Resources (UCAR). Sources of animals used in this study were as previously described (Seluanov et al., 2007; Seluanov et al., 2008). C57BL/6 mice were purchased from the Jackson Laboratory. Two mice were caught in New York State. Brown Norway rats, BN/Crl, and Fischer 344 rats, F344/IcoCrl, were purchased from Charles River Laboratories. Outbred Mongolian gerbils, Crl:MON(Tum), and outbred golden hamsters, Crl:LVG(Syr), were purchased from Charles River Laboratories. Capybaras were obtained from Bio Fau Assesoria e Comercio (São Paulo, Brazil). Pacas were from the animal facility at São Paulo State University. Outbred multicolored guinea pigs were purchased from Elm Hill Labs. Chinchillas were purchased from Moulton Chinchilla Ranch. Beavers, deer mice, woodchucks, chipmunks, porcupines, red, and gray squirrels were trapped in New York State. Fox squirrels were trapped in Ohio. Blind mole rats were caught in Upper Galilee Mountains in Israel. Naked mole rats were from the colonies at University of Rochester.

Drosophila

All the *UAS-Sirt6* transgenic fly lines were generated by PhiC31 integrase-based transgenesis, integrating into the attP40 landing site (BestGene, CA). The Actin-GeneSwitch-Gal4 flies which expresses a progesterone-inducible GAL4 ubiquitously (Osterwalder et al., 2001) were courtesy of Dr. Benoit Biteau from University of Rochester Medical Center. All the flies were maintained on standard fly food at 18°C as lab stocks and at 25°C for experiments.

Primary cell cultures

Primary fibroblasts were isolated from under-arm skin and lung tissues as previously described (Seluanov et al., 2010b). Briefly, skin tissues were shaved and cleaned with 70% ethanol. Lung tissues were rinsed with PBS to get rid of excess blood. Tissues were minced and incubated in DMEM/F-12 medium (ThermoFisher, 11320033) with Liberase TM (Sigma, 5401127001) at 37°C on a stirrer for 15-90 min. Tissues were then washed and plated with DMEM/F-12 medium containing 15% fetal bovine serum (GIBCO) and Antibiotic-Antimycotic (GIBCO). When cells are ~80% confluent, isolated cells were frozen in liquid nitrogen within 2 passages. All subsequent cultures were performed in EMEM (ATCC, 30-2003) supplemented with 15% fetal bovine serum (GIBCO), 100 units/mL penicillin, and 100 μg/mL streptomycin (GIBCO). All primary cells were cultured at 37°C with 5% CO_2 and 3% O_2 except naked mole-rat cells, which were cultured at 32°C with 5% CO_2 and 3% O_2.

Cell lines

HEK293T/17 cells were purchased from ATCC and maintained in DMEM containing 10% fetal bovine serum and 1% penicillin-streptomycin at 37°C with 5% CO_2 and 3% O_2.

METHOD DETAILS

Host cell reactivation assay

Host cell reactivation assay was used to measure the repair of UV-induced DNA damage. UV-induced DNA lesions are also able to be converted to DNA DSBs during DNA replication by causing collapsed replication forks (Batista et al., 2009). However, the FFL plasmid lacks a eukaryotic replication origin and cannot replicate in rodent cells, ensuring that our assay is specific to measure NER.

One mL of a firefly luciferase (FFL) plasmid, pCMV-Luc, at a concentration of 0.5 μg/μL was aliquoted into 25 μL droplets in a 10 cm plate and irradiated with 400 or 1200 J/m^2 of 254nm UV light with lid open. The same batch of UV-treated plasmids was used for testing all species to avoid batch-to-batch variation. 1 × 10^6 cells were co-transfected with 1 μg of treated pCMV-Luc plasmid and 0.04 μg intact Renilla luciferase plasmid pRL-CMV (Promega). Transfections were done with program U-20 using an Amaxa Nucleofector II machine. 48 h after transfection, cells were lysed and luciferase activity was measured using Dual-Luciferase Reporter Assay System (Promega). A ratio between firefly luciferase activity and Renilla luciferase activity was calculated to normalize the data. The percentage of repaired DNA was calculated by the recovery of normalized firefly luciferase activity at each UV dose compared with the untreated control. For each cell line, three technical replicates were performed for each UV dose.

UV sensitivity assay and calculation of LD50

Cells were UV irradiated at confluency. Once becoming confluent, the cells in 6cm plates were washed with phosphate-buffered saline (PBS) and irradiated with 254 nm UV light in 5 mL PBS with the lid open. Each plate of a cell line was exposed to serial doses of 0, 25, 50, 100, 200, 400, 800, 1200, or 2400 J/m^2. Cells from multiple species receiving the same dose were treated together to minimize variations. Cells from each species were tested in triplicate at each dose. PBS was removed after irradiation and complete medium was added back. Cells were then cultured for 3 days before cell survival was measured by metabolic conversion of WST-1 (Roche).

To calculate LD50, the survival percentage at each dose was calculated as the proportion of WST-1 conversion relative to the untreated control. An exponential regression of the cell survival in the function of UV dose was fitted to each cell line. The regression coefficient (r^2) between 0.95 and 0.99 was usually achieved. LD50 was then calculated based on the regression equation of each cell line.

Generation of NHEJ and HR reporter cell lines

NHEJ and HR reporter constructs were digested with NheI restriction enzyme and purified with the QIAEX II gel extraction kit (QIAGEN). The same batch of DNA preparation was used for generating all reporter cell lines of rodent species. Young cells (population doubling < 10) were recovered from liquid nitrogen and passaged once before integration of the constructs. 0.5 μg of linearized NHEJ and HR constructs were electroporated into each cell line. Two days after transfection, media was refreshed and G418 was applied for selection of the stable clones. Triplicates of each reporter in each cell line were prepared to obtain an adequate number of stable clones. 40-100 clones were generated from each transfection. Clones from triplicate plates were pooled to get at least 100 clones per reporter per cell line. During this process, skin fibroblasts from paca, woodchuck and fox squirrel and lung fibroblasts from paca, gray squirrel, and porcupine gave rise to senescent clones and were not included in further analysis.

DSB repair assays and FACS analysis

In vivo DSB repair assays were performed as previously described (Mao et al., 2011). Briefly, growing cells were co-transfected with 5 μg of plasmid encoding I-SceI endonuclease and 0.025 μg of plasmid encoding DsRed. The same batch of I-SceI and DsRed mixture was used throughout all species to avoid batch-to-batch variation. Two human fibroblast cell lines containing clonally integrated NHEJ and HR reporter constructs used previously (Mao et al., 2011) were included for each experiment. DSB repair efficiency of these two reference cell lines is consistent throughout the experiments. To test the effect of SIRT6 on DSB repair, SIRT6 plasmids were co-transfected with I-SceI and DsRed plasmids. Three days after transfection, the numbers of GFP+ and DsRed+ cells were determined by flow cytometry on a FACS Canto machine (BD Biosciences). For each sample, a minimum of 20,000 cells were analyzed. DSB repair efficiency was calculated by dividing the number of GFP+ cells by the number of DsRed+ cells.

Cloning Sirt6 from rodents and mutagenesis

Sirt6 genes from 7 species including mouse (NM_181586), rat (NM_001031649), golden hamster (XM_005083238), deer mouse (XM_006978115), chinchilla (XM_013505251), naked mole rat (NM_001310264), and blind mole rat (XM_017799169.1) have been annotated and deposited in GenBank. The coding sequence (CDS) of *Sirt6* genes from these 7 species were amplified by RT-PCR using mRNA prepared from young cells (PD < 10) of the corresponding species and sequenced to verify the correct cloning. *Sirt6* CDS were then cloned into pEGFP-N1 plasmid in which EGFP was replaced. *Sirt6* genes of the other rodent species including gerbil, guinea pig, paca, capybara, porcupine, red squirrel, woodchuck, chipmunk, gray squirrel, and beaver were cloned by rapid amplification of cDNA

ends (RACE). Degenerate primers designed based on the conserved regions of SIRT6 were used to amplify the internal sequences. Species-specific primers were then designed based on the internal sequences and used in RACE to amplify both 3′ and 5′ end of the *Sirt6* cDNA. Full length *Sirt6* CDS were finally amplified and cloned into pEGFP-N1 plasmid in which EGFP was replaced.

Mutagenesis of mouse and beaver *Sirt6* genes was performed in multiple ways. Fusion protein mutants which incorporate a long sequence or multiple sites of the opposite species were generated by DNA synthesis of the mutated regions which were then swapped back into the wild-type *Sirt6* genes using KpnI/NotI for mouse *Sirt6* and SbfI/NotI for beaver *Sirt6*. Single mutants were generated using Quickchange II site directed mutagenesis kit (Agilent) by PCR (Table S5). The sequences were verified by Sanger sequencing.

Immunofluorescence and foci quantification

Confluent cells from both short- and long-lived species were treated with 8 Gy of γ-radiation, after which DNA damage foci were stained with γ-H2AX and 53BP1 antibodies and quantified at 1h and 24h. Considering the potential non-specificity of γ-H2AX and 53BP1 antibodies across species, we used co-localized foci as a more reliable indication of DNA damage (Figure S4A).

Fibroblasts were grown on Lab-Tek II Chamber Slides (ThermoFisher Scientific) until reaching confluency, followed by 8 Gy of γ-irradiation. After treatment, cells were fixed at different time points and processed for immunofluorescence. 5-ethynyl-2′-deoxyuridine (EdU) was added 30 min before fixation and stained using the Click–iT Plus EdU Imaging Kit (ThermoFisher Scientific, C10640) to confirm the cell cycle arrest. EdU staining was performed according to the manufacturer's recommendations. Briefly, the cells were fixed in 4% formaldehyde in PBS for 15 min at RT, after which, cells were rinsed twice with 3% BSA solution in PBS, permeabilized with 0.5% Triton X-100 in PBS for 20 min at room temperature, washed with 3% BSA in PBS and then treated with reagents of Click-iT cocktail including Azide-Alexa Fluor 647 triethyl ammonium salt in the dark for 30 min.

Following EdU labeling, cells were blocked for 1 h at room temperature in 1% Blocking Reagent (Roche, 11096176001) in PBST. For experiments in different species, cells were incubated with mouse monoclonal anti-γH2AX (Millipore, 05-636, 1:500) and rabbit polyclonal anti-53BP1 antibodies (Abcam, ab172580, 1:500) at +4°C overnight. For SIRT6 overexpression experiments, cells were incubated with mouse monoclonal anti-FLAG (Sigma, F3165, 1:500) and rabbit polyclonal anti-γH2AX antibodies (abcam, ab11174, 1:500) at +4°C overnight. All antibodies were diluted in 0.5% Blocking Reagent solution. After incubation with primary antibodies, cells were washed in PBST three times and incubated with goat anti-rabbit (Alexa Fluor 568) and goat anti-mouse antibodies (Alexa Fluor 488) (ThermoFisher Scientific, 1:400) for 1 h at room temperature. Afterward, slides were mounted in VECTASHIELD Antifade Mounting Medium with DAPI. Images were taken using the Leica TCS SP5 Confocal system. Confocal images were collected with a step size of 0.5 μm covering the depth of the nuclei. Far-red, red, green, and blue fluorescence were acquired sequentially to avoid bleed-through artifacts.

To count foci, Z stacks of confocal sections were collected, and maximal projections of the series were obtained. Co-localized γH2AX/53BP1 foci in control cells and 24 h samples after irradiation were counted by eye. The foci in 1 h samples were counted using FoCo (Lapytsko et al., 2015), and parameters were adjusted according to the authors' recommendations.

CRISPR/Cas9-mediated knockout of SIRT6

CRISPR gRNAs were designed using sgRNA Scorer 2.0 and synthesized at Integrated DNA Technologies. The annealed gRNA1 and gRNA2 (Table S3) were inserted into Bbs1-digested pSpCas9(BB)-2A-Puro (PX459) plasmid (Addgene plasmid # 62988) to generate PX459-hSIRT6 gRNA1 and PX459-hSIRT6 gRNA2. The plasmids were sequenced to verify the sequence.

To generate SIRT6 knockout human dermal fibroblasts, primary human dermal fibroblasts were first immortalized with a piggyBac vector expressing *hTERT* (Tian et al., 2018) and selected with 1 mg/mL G418 (ThermoFisher). The immortalized cells were co-transfected with PX459-hSIRT6 gRNA1 and PX459-hSIRT6 gRNA2 plasmids and plated sparsely to form colonies in 2 weeks. Colonies were picked and genomic DNA was extracted to perform genotyping PCR. The sequences of the genotyping primers are as follows: F1: 5′-CCGCATTTTAGAGGTGACTGGAG-3′, R1: 5′-CTAGACCCTGACAGCTCTCCTCC-3′; F2: 5′-GACAAGCT GCCTTTTCCAATCCA-3′, R2: 5′-AGGAGGAAAGCAGATGGATGTGT-3′. If the sequence between gRNA1 and gRNA2 is successfully deleted by CRISPR, PCR with the F1 and R1 primers will produce a 400bp band, whereas PCR using the F2 and R2 primers will not amplify anything. F2 and R2 primers will amplify a 367bp band in WT cells. The successfully edited clones were verified using western blotting and used for subsequent experiments.

Construction of lentiviral overexpression vectors

The coding sequences (CDs) for mouse WT, mouse 5mut, beaver WT, and beaver 5mut SIRT6 were amplified by PCR using the following primers: pLJM1-mouse *Sirt6* primers (Table S5) for mouse WT and mouse 5mut *Sirt6*, and pLJM1-beaver *Sirt6* primers (Table S5) for beaver WT and beaver 5mut *Sirt6*. The amplified fragments were digested with Age1 and EcoR1, and then inserted between the Age1 and EcoR1 sites of pLJM1-EGFP (Addgene plasmid # 19319). The sequences were verified by Sanger sequencing.

Construction of lentiviral miRNA vectors

To knockdown SIRT6 in beaver fibroblasts, we used lentivirus-delivered shRNA. shRNA sequences were designed using Genetic Perturbation Platform (Broad Institute, USA) and BLOCK-iT RNAi Designer (ThermoFisher Scientific). Each pair of oligos (Table S4) were annealed and inserted between the AgeI and EcoRI sites of pLKO.1 hygro (Addgene plasmid # 24150). The sequences were verified by Sanger sequencing.

Lentiviral production and transduction

Lentiviral particles were produced in HEK293T/17 cells (ATCC, CRL-11268) using a Lenti-X Packaging kit (Takara, 631275). To transduce pLJM1-based SIRT6 overexpression lentivirus into SIRT6 knockout human dermal fibroblasts, a serial dilution of each lentivirus was transduced in the presence of 10 μg/mL polybrene. Cells were selected with 1 μg/mL puromycin. Control cells were included to ensure the complete death of un-transduced cells. The expression level of SIRT6 was quantified by western blotting. Cells expressing a similar level of different SIRT6 were used for further experiments.

To knockdown *Sirt6* in beaver skin fibroblasts, pLKO.1-based shRNA lentiviruses were transduced in the presence of 10 μg/mL polybrene. Three days after transduction, cells were selected with 100 μg/mL hygromycin. Control cells were included to ensure the complete death of un-transduced cells. The knockdown efficiency was tested by western blotting.

Clonogenic assay

Clonogenic assay was performed according to a previously published protocol (Franken et al., 2006) with minor modifications. Basically, cells received γ-radiation at 0, 1, 2, 3, 4, 6, and 8Gy when they were confluent. Serial dilutions of irradiated cells were plated immediately after irradiation. Cells were incubated until the colonies formed, which takes 2-3 weeks except the naked mole rat cells, which take 6-8 weeks. Colonies were fixed and stained in a solution containing 6.0% glutaraldehyde and 0.5% crystal violet and counted by two investigators. Cell survival after each dose of radiation was expressed as the relative plating efficiencies of the irradiated cells to that of the control cells. To calculate the LD50 and LD75, the linear-quadratic model was used to fit the survival data against the radiation dose (Bodgi et al., 2016). Analyses were performed using Graphpad Prism software.

Senescence-associated β-galactosidase (SA-β-gal) staining

Human dermal fibroblasts expressing similar levels of SIRT6 proteins were γ-irradiated at 0, 5, and 10 Gy. Ten days after radiation, cells were splitted to be ~40% confluent to avoid false-positive staining due to confluency. SA-β-gal staining was performed two days after splitting according to the Campisi lab's protocol (Debacq-Chainiaux et al., 2009; Dimri et al., 1995). Basically, cells were washed twice with PBS and fixed in a solution containing 2% formaldehyde and 0.2% glutaraldehyde in PBS for 5 min at room temperature. After fixation, cells were immediately washed twice with PBS and stained in a solution containing 1 mg/mL 5-bromo-4-chloro-3-indolyl P3-D-galactoside (X-Gal), 40 mM citric acid/sodium phosphate buffer, pH 6.0, 5 mM potassium ferrocyanide, 5 mM potassium ferricyanide, 150 mM NaCl, and 2 mM $MgCl_2$. Plates were incubated at 37°C for 16 h without CO_2. Colorimetric images were taken from different areas of each plate and quantified by a researcher that was blinded to the treatments.

Protein purification

The ORFs of mouse WT, mouse 5mut, beaver WT and beaver 5mut SIRT6 were cloned into the backbone of pET11a vector (Novagen) using NdeI and BamHI (Table S5). Expression vectors were transformed into Rosetta-gami B(DE3)pLysS competent cells (Novagen, 71137-4) and plated on LB agar with ampicillin, kanamycin, tetracycline, and chloramphenicol (AKTC) antibiotics. Single colonies were inoculated in LB medium supplemented with AKTC, and the overnight culture was expanded into 2L AKTC LB medium. When the OD600 reached 0.6-0.8, 1 mM IPTG was added to induce protein production for 3 h at 37°C. The 6 × His-tagged proteins were purified with Ni-NTA beads (ThermoFisher Scientific, R90115).

Histone deacetylation assays

In vitro deacetylation reactions were performed as described in (Gil et al., 2013; Michishita et al., 2008), with some modifications. 2.5 μM (~5 μg) of each recombinant SIRT6 protein was incubated with 2 μg purified HeLa polynucleosomes (EpiCypher, 16-0003) in 50 μL deacetylation buffer (50 mM Tris-HCl, pH 8.0, 2mM NAD+, 150 mM NaCl, 4 mM $MgCl_2$, 10 μM $ZnCl_2$, and 1 mM DTT) for 3 h at 30c°C. After incubation, Laemmli buffer was added, and samples were boiled for 10 min. Histone acetylation levels after reactions were detected using western blot analysis with acetylation specific antibodies.

ADP-ribosylation assay

The reactions analyzing mono-ADP-ribosylation activity were performed as described previously (Liszt et al., 2005; Mao et al., 2011), with minor modifications. Reactions containing 2.5 μM (~5 μg) of each recombinant SIRT6 protein in 50 μL of 50 mM Tris-Cl, pH 8.0, 150 mM NaCl, 10 μM $ZnCl_2$, 10 mM DTT, 25 μM unlabeled NAD+ and 8 μCi ^{32}P NAD+ (PerkinElmer, NEG023X250UC) were incubated at 37c°C for 3 h. Samples were then resuspended in Laemmli buffer, and boiled for 10 min. The samples were resolved in SDS-PAGE gels and transferred to polyvinylidene difluoride membrane before autoradiography.

The stimulation of PARP1 activity by mouse WT SIRT6, beaver WT SIRT6, and their mutants was performed as in (Mao et al., 2011). Briefly, 2.5 μM (~5 μg) of recombinant SIRT6 proteins were incubated with 1 μg PARP1 (Sigma, P0996) in 50 μL of PARP1 reaction buffer (50 mM Tris-Cl, pH8.0, 150 mM NaCl, 4 mM $MgCl_2$, 10 μM $ZnCl_2$, 1 mM DTT, 400 μM NAD+, and 0.1 μg/mL sonicated fish sperm DNA) at 30c°C for 30 min. PARP1 activity was detected by western blotting with anti-PADPR antibody.

Thermal denaturation assay

Thermal Denaturation assays were used to determine the melting temperature (T_m) of the mouse WT, mouse 5mut, beaver WT, and beaver 5mut variants of SIRT6. Purified proteins were diluted to 10 μM in a buffer (150 mM NaCl, 50 mM Tris pH 7.4, 5% glycerol)

containing 2.5 × SYPRO orange dye (ThermoFisher, S6650). Samples were then aliquoted into 50 μl reaction wells and analyzed in a Bio-Rad CFX Connect Real-Time PCR Detection System. Samples were heated from 10°C to 95°C at a gradient of 0.5°C/min. Fluorescence intensities were measured using the FRET channel and measurements were taken every 0.5°C. At least three replicates were performed for each SIRT6 variant. Each thermal denaturation curve was then normalized so that maximum fluorescence was equal to 1 and minimum fluorescence was equal to 0. The curves were then fitted to the following equation, as previously used in (Kugel et al., 2015), to obtain the T_m.

$$I = \left(\frac{1}{1 + e^{\left(\frac{T_m - T}{C} \right)}} \right)$$

Where I is the normalized fluorescence intensity at temperature T and C is a slope factor.

SIRT6 de-myristoylation assay

SIRT6 de-myristoylase (de-MYR) activity was determined using a previously described approach using a myristoylated TNF-α peptide (MYR peptide) identical to peptide **3** in Schuster et al. (Schuster et al., 2016). In this assay, de-MYR activity is manifest as in increase in fluorescence over time due to the loss of fluorescence quenching of a fluorophore located at the end of the myristoyl group by a neighboring 3-nitrotyrosine group on the peptide (Schuster et al., 2016). The peptide we employed was custom synthesized by Genscript (Piscataway, NJ) and its mass was confirmed by matrix-assisted laser desorption ionization time-of-flight mass spectrometry (MALDI-TOF MS). All de-MYR measurements were performed for 30 min in 25 μL final volume in Greiner 384 well low volume black plates using a Spark 20 M plate reader (Tecan; Männedorf, Switzerland) with λ Ex = 310 nm and λ Em = 405 nm. In all cases 500nM SIRT6 protein was incubated in 50mM Tris-HCl pH 7.5, 150mM NaCl, 10 mM β-mercaptoethanol, and 5% glycerol. When varied, NAD^+ and MYR peptide were indicated in the figure legend. When NAD^+ was varied, MYR peptide was held constant at 90 μM. When MYR peptide was varied, NAD^+ was held constant at 500 μM. De-MYR rates were calculated from the increase in relative fluorescence per second for a period of 10 min where the rate was linear. Kaleidagraph software was used to fit de-MYR rates to the Michaelis-Menten equation to obtain K_M and V_m for either NAD or MYR-peptide. Measurements for the entire group of beaver or mouse alleles were performed together, allowing us to directly compared relative fluorescence unit (rfu) changes directly. Since rfu values are comparable, and we added and an identical amount of each SIRT6 protein to each reaction, we present V_m/K_M values as a proxy for the more traditional k_{cat}/K_M.

Pulse-chase assays

One day after transfection with SIRT6 expressing vectors, adherent cells in 10 cm dish where washed twice in PBS and incubated for 30 min in pulse-labeling medium (DMEM, methionine/cysteine-free and containing 12% dialyzed FBS) to deplete intracellular pools of methionine and cysteine. After the medium was removed, cells were incubated for 1h in a labeling cocktail: Express Protein Labeling Mix [^{35}S] (PerkinElmer) in pulse-labeling medium prepared just before use by adding 200 μCi of [^{35}S] labeling mix in the medium per dish. After labeling, the cocktail was quickly removed and cells were washed twice in PBS and incubated for various time periods in Eagle's Minimum Essential Medium (EMEM) (ATCC). At desired time points, cells were harvested and subjected to immunoprecipitation procedure. Briefly, cells were lysed in IP buffer (20 mM HEPES pH8, 0.2 mM EDTA, 5% glycerol, 150 mM NaCl, 1% NP-40, protease inhibitor cocktail) for 10 min on ice, and after sonication and centrifugation at 13000rpm at 4°C, lysates were precleared for 1h with Pierce Protein A Agarose (ThermoFisher Scientific), followed by overnight incubation with 3 μg of anti-Sirt6 antibodies (Abcam, ab62739). Lysates were then incubated for 3h with Protein A Agarose, and after 5 washes with IP buffer, immune complexes were eluted with 2x Laemmli sample buffer (BioRad), heated for 10 min at 95°C and loaded on 4%–20% SDS-PAGE gel. After electrophoresis, gels were dried for 2h in gel-drier and exposed to Carestream Kodak BioMax MS films for 9 days before development.

Protein structure analysis

Mouse WT SIRT6 and its mutant with the five beaver amino acid substitutions were modeled with the SWISS-MODEL program (Biasini et al., 2014) based on a human SIRT6 structure (PDB code: 3ZG6). The two predicted crystal structures were very similar, which were super-imposed for visualization using the UCSF Chimera (Pettersen et al., 2004).

In vitro co-immunoprecipitation assay

In vitro co-immunoprecipitation experiment was used to measure the binding affinity of purified SIRT6 proteins to nucleosomes. 0.25 μM (~1 μg) of each recombinant SIRT6 protein was incubated with 0.1 μM (~2.1 μg) HeLa mononucleosomes in 100 μL nucleosome binding buffer (20 mM HEPES pH 8.0, 80 mM KCl, 0.1 mM $ZnCl_2$, 0.1% EDTA, 10% glycerol, 0.1% NP40, 0.5 mM DTT) for 20 min at RT. After incubation, 10 μL of each sample was saved to use as input control, and 400 μL IP buffer (20 mM HEPES pH8.0, 0.2 mM EDTA, 5% glycerol, 150 mM NaCl, 1% NP40) supplemented with protease inhibitor cocktail (Roche, 04693132001) and 0.25 μM (~4 μg) anti-SIRT6 antibody (Abcam, ab62739) were added to each sample. Following rotating at 4°C overnight, 100 μL protein A/G agarose (ThermoFisher Scientific, 20421) was added and tubes were rotated at 4°C for another 2 h. Beads were then

collected by centrifugation for 1 min at 8,000 rpm at 4°C and washed 5 times with IP buffer. Proteins were eluted with 2x Laemmli sample buffer (BioRad) and boiled for 10 min. The supernatant after centrifugation was used for western blotting analysis.

Fly lines, husbandry, and lifespan assays

All the *UAS-Sirt6* transgenic fly lines were generated by PhiC31 integrase-based transgenesis, integrating into the attP40 landing site (BestGene, CA). The coding sequence of mouse WT, beaver WT, and their mutant Sirt6 was amplified by PCR (Table S5) and inserted into the EcoR1 and Not1 sites of pUAST-attB (Sykiotis and Bohmann, 2008) to generate pUAS-Sirt6 plasmids, which express different versions of Sirt6 under the control of the Gal4 responsive promoter sequence, the Upstream Activating Sequence (UAS). Empty vector was used to generate the control fly line. The Actin-GeneSwitch-Gal4 flies which expresses a progesterone-inducible GAL4 (Osterwalder et al., 2001) ubiquitously were courtesy of Dr. Benoit Biteau from University of Rochester Medical Center. All the flies were maintained on standard fly food at 18°C as lab stocks and at 25°C in preparation for experiments.

RU486 (mifepristone) was used to induce the activation of Gal4. In experiments using RU486 treatment, 10 mM RU486 (Cayman Chemical, 10006317) was prepared in 80% ethanol and mixed with standard fly food at 50°C. 100 μM RU486 containing food was used for long-term treatment (the lifespan assay) while 320 μM RU486 food was used for short-term treatment (4-day treatment in the western blot assay). A corresponding amount of ethanol was added to the control food.

The SIRT6 protein abundance was measured by SDS-PAGE gel electrophoresis and western blotting. In each experiment, 4 flies were collected and homogenized with small pestles fitting into 1.5 mL test tubes using a pestle motor (Kontes, USA) in 300 μL ice-cold RIPA buffer with 1x protease inhibitor cocktail (ThermoFisher, A32965) and phosphatase inhibitor (Roche, 4906845001). The protein samples were incubated on a rotator for 1.5h at 4°C. 100 μL 4x Laemmli sample buffer (Bio-Rad, 1610747) was then added to each protein lysate sample. The lysate was boiled for a total of 10min. 20 μL protein lysate from each sample was loaded for SDS-PAGE gel electrophoresis.

To conduct the lifespan assays, male *UAS-Sirt6* flies were crossed with virgin female *Actin-GeneSwitch-Gal4* flies. The F1 flies were collected at the age of 0 to 1 day post eclosion. Only the F1 flies were used to ensure that the genetic background of the tested flies is the same across different *Sirt6* lines. Males and females were kept together overnight to ensure the same mating status of the flies being tested. They were then separated by sex and subjected to control or RU486 treatment. In each treatment group, a total number of 320 to 360 flies were collected and distributed into 6 bottles of control or RU486 food (about 50 to 60 flies/bottle). All the flies were kept at consistent temperature (24 ± 2°C) and humidity (55% - 70%) with a 12:12 h light - dark cycle during the aging process and were transferred to fresh food three times per week. Flies were scored as live or dead twice per week during the first 7 weeks and three times per week at later stage until the last survivor was dead. Statistical tests were performed on the survivorship data using OASIS 2 (Han et al., 2016).

QUANTIFICATION AND STATISTICAL ANALYSIS

Data are presented as the mean ± SEM or SD. Statistical tests were performed using Student's t test or one-way ANOVA with Tukey's post hoc test. p values of less than 0.05 were considered statistically significant. Statistical analyses were carried out using GraphPad Prism software unless otherwise stated. Statistical details can be found in the figure legends and Results. Phylogenetically independent contrast analysis and phylogenetic ANOVA were used to correct the effect of phylogenetic relationship of the rodents on comparative analyses. The detailed methods are described below.

Phylogenetically independent contrast analysis

Closely related species share common ancestry (phylogenetic non-independence) and, therefore, cannot be treated as statistically independent when subjected to comparative analyses (Felsenstein, 1985). In order to correct for the influence of phylogenetic relatedness, we performed phylogenetically independent contrast analyses. Briefly, the PDAP package was used for the analysis and run in Mesquite program (Garland et al., 1993). The information of rodent phylogeny and divergence time (Figure 1) was obtained from (Fabre et al., 2012; Meredith et al., 2011).

Phylogenetic ANOVA

Phylogenetic ANOVA was performed to correct the phylogeny effect in ANOVA analysis. The same phylogeny tree from Figure 1 was used in all phylogenetic analyses across this study. The tree was read into R (version 3.2.3, 64 bit) with the Ape package (Paradis et al., 2004) as provided by the Bioconductor project (Gentleman et al., 2004). The phylanova method from the PhyTools package (Revell, 2012) was used for phylogeny-independent testing, using 100,000 simulation iterations, post hoc testing enabled, and Benjamini-Hochberg multiple testing adjustment of p values.

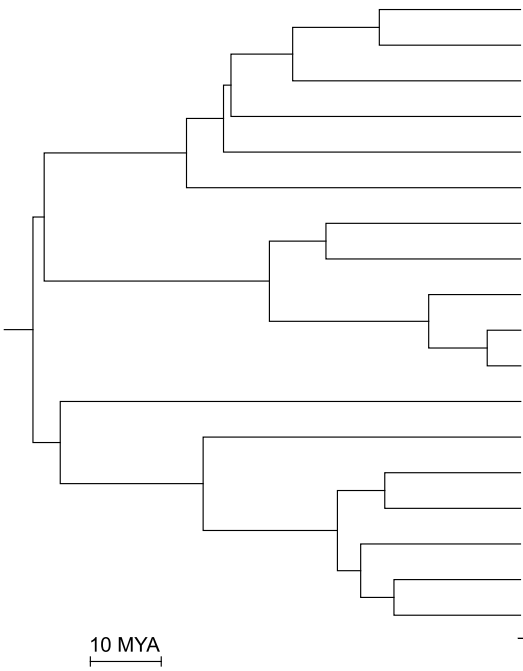

Common name	Scientific name	Maximum lifespan (yr)	Adult body mass (g)
Guinea pig	*Cavia porcellus*	12	728
Capybara	*Hydrochoerus hydrochaeris*	15	55,000
Paca	*Cuniculus paca*	16	9,000
N. American porcupine★	*Erethizon dorsatum*	23	8,600
Chinchilla	*Chinchilla lanigera*	17	642
Naked mole-rat★	*Heterocephalus glaber*	32	35
Woodchuck	*Marmota monax*	14	5,000
Eastern chipmunk	*Tamias striatus*	10	96
American red squirrel	*Tamiasciurus hudsonicus*	10	200
Fox squirrel	*Sciurus niger*	16	800
Eastern grey squirrel★	*Sciurus carolinensis*	24	533
American beaver★	*Castor canadensis*	24	20,250
Blind mole-rat★	*Nannospalax ehrenbergi*	21	160
Golden hamster	*Mesocricetus auratus*	4	105
Deer mouse	*Peromyscus maniculatus*	8	20
Mongolian gerbil	*Meriones unguiculatus*	6	53
House mouse	*Mus musculus*	4	30
Norway rat	*Rattus norvegicus*	5	400

Figure S1. Phylogeny, Maximum Lifespan, and Body Mass for 18 Rodent Species, Related to Figures 1–4

Maximum lifespan and adult body mass data were obtained from the Animal Aging and Longevity Database (Tacutu et al., 2013). The tree topology and divergence time were derived from (Fabre et al., 2012; Meredith et al., 2011). Red stars indicate slow-aging species with maximum lifespan > 20 years.

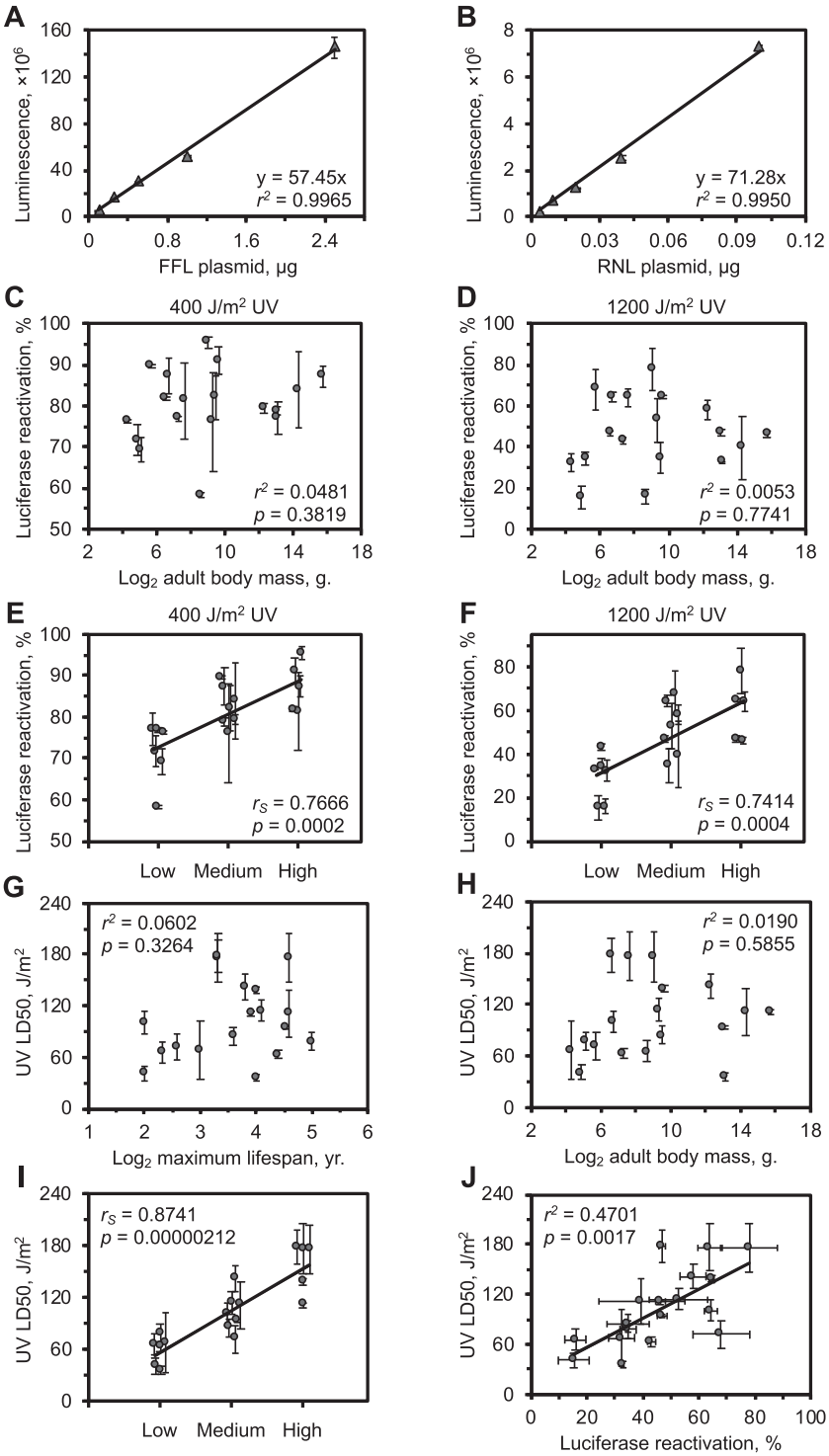

Figure S2. NER Efficiency and UV Resistance Correlate with the Level of Sunlight Exposure in Rodent Species, Related to Figure 1

(A and B) Luciferase activity is proportional to the amount of transfected plasmid for both (A) FFL and (B) RNL plasmids. Error bars indicate SD from three repeats. *r*, Pearson correlation coefficient.

(C and D) Luciferase reactivation of UV-damaged FFL plasmid at (C) 400 J/m^2 or (D) 1200 J/m^2 does not correlate with adult body mass. The data from Figure 1B, C were used for the statistical analysis. Error bars indicate SEM *r*, Pearson correlation coefficient. p-values were determined by Student's t test for Pearson correlation.

(legend continued on next page)

(E and F) NER efficiency positively correlates with the level of sunlight exposure. The data from Figure 1B, C were used to perform the Spearman's rank correlation test against the rank of sunlight exposure. Data points were scattered for better visualization. r_S, Spearman's rank correlation coefficient. p values were determined by Student's t test for Spearman's rank correlation. Error bars indicate SEM.

(G and H) UV LD50 does not correlate with (G) species maximum lifespan or (H) adult body mass. On average, cells isolated from 3 different animals of each species were used. Each circle in the plots represents a species. Error bars indicate SEM r, Pearson correlation coefficient. p values were determined by Student's t test for Pearson correlation.

(I) UV LD50 positively correlates with the level of sunlight exposure. The data from Figures S2G and S2H were used to perform the Spearman's rank correlation test against the level of sunlight exposure. Data points were scattered for better visualization. r_S, Spearman's rank correlation coefficient. p values were determined by Student's t test for Spearman's rank correlation. Error bars indicate SEM.

(J) UV LD50 significantly correlates with NER efficiency. UV LD50 was plotted against the luciferase reactivation of UV-damaged FFL plasmid at 1200 J/m^2. *r*, Pearson correlation coefficient. p values were determined by Student's t test for Pearson correlation. The phylogenetically corrected data are described in the main text. Error bars indicate SEM.

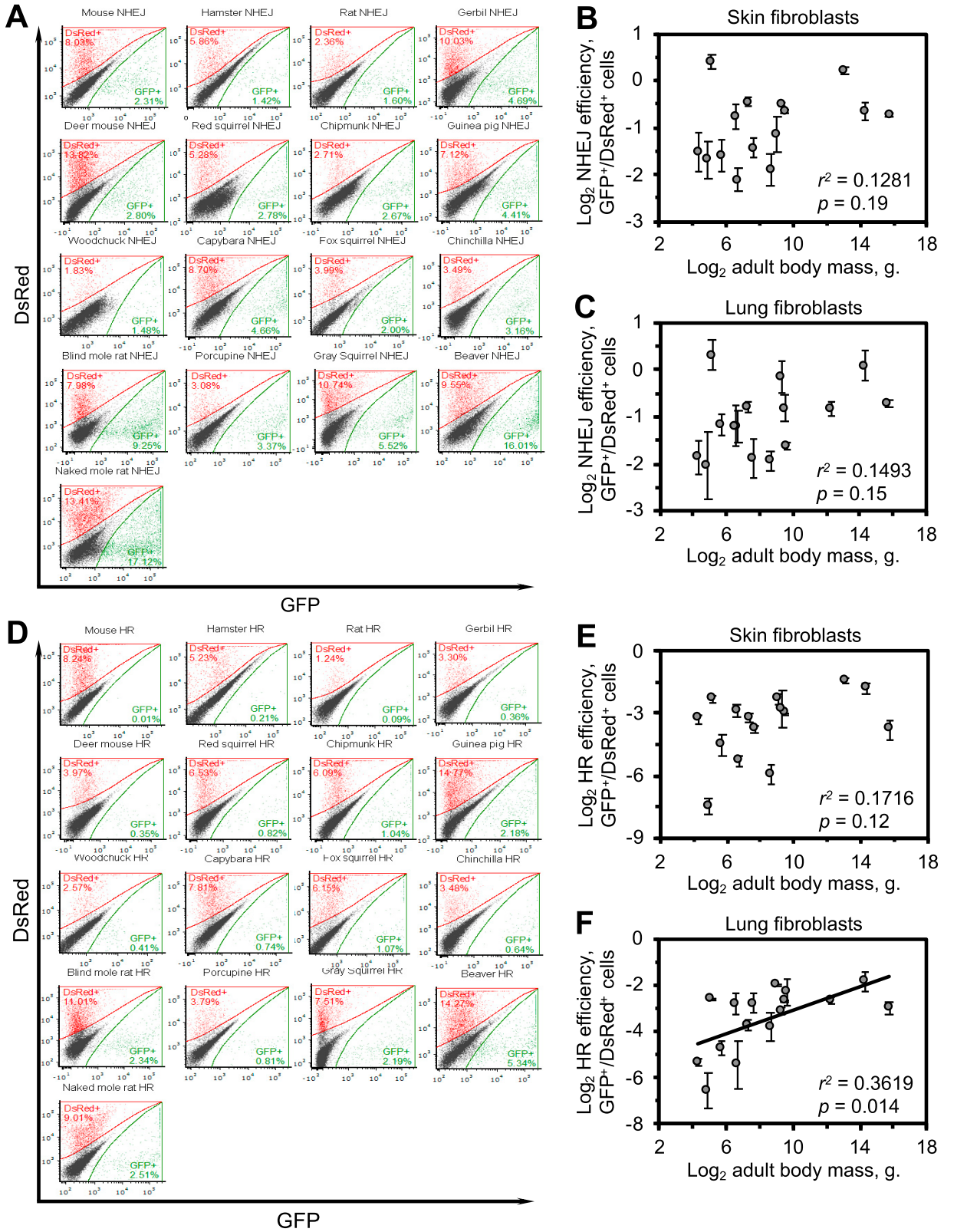

(legend on next page)

Figure S3. Efficiency of DNA DSB Repair Does Not Correlate with Adult Body Mass, Related to Figure 2

(A) Representative flow cytometry images for the NHEJ repair assays in rodent cells.

(B and C) NHEJ repair efficiency does not correlate with adult body mass in either (B) skin fibroblasts or (C) lung fibroblasts. Statistical significance was calculated for phylogenetically corrected data: (B) $r^2 = 0.0053$, p = 0.80; and (C) $r^2 = 0.048$, p = 0.43.

(D) Representative flow cytometry images for the HR repair assays in rodent cells.

(E) HR repair efficiency in skin fibroblasts does not correlate with adult body mass. After phylogenetic correction, $r^2 = 0.0063$, p = 0.78.

(F) HR repair efficiency in lung fibroblasts significantly correlates with adult body mass. But the significance was lost after correction for phylogenetic non-independence ($r^2 = 0.17$, p = 0.11).

The data for DSB repair efficiency from Figures 2D–2G were used to test for the correlation between DSB repair efficiency and adult body mass of the corresponding species. Error bars represent SEM *r*, Pearson correlation coefficient. p values were determined by Student's t test for Pearson correlation.

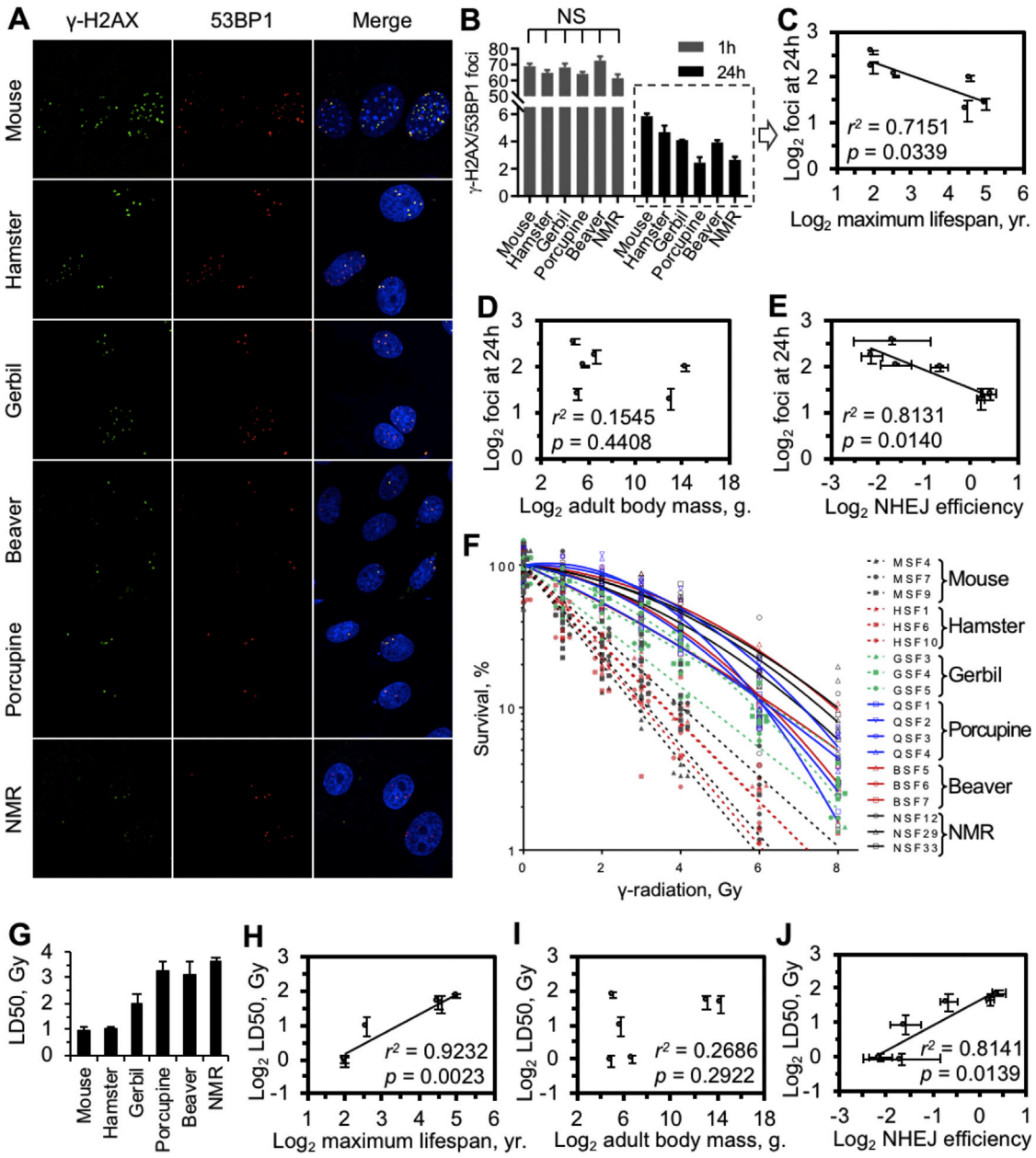

Figure S4. Cells from Long-Lived Species Have More Efficient DSB Repair, Related to Figure 2

(A) Representative fluorescent micrographs of cells stained for γ-H2AX and 53BP1 in rodent cells at 24 h after 8 Gy of γ-irradiation.

(B) Quantification of DNA damage foci. Co-localized γ-H2AX and 53BP1 foci were quantified. Background levels of co-localized foci (average < 1) were subtracted from the foci number at both 1h and 24h. Two to three cell lines of each species were used, and more than 50 nuclei of each cell line were analyzed at each condition. Error bars represent SEM.

(C and D) Unrepaired DNA damage at 24 h after γ-irradiation, represented by the number of co-localized γ-H2AX and 53BP1 foci, negatively correlates with species maximum lifespan, but not body mass. Data from (B) at 24 h was used to test the correlation. r, Pearson correlation coefficient. p-values were determined by Student's t test for Pearson correlation.

(E) Negative correlation between unrepaired DNA damage and NHEJ efficiency measured in Figure 2.

(F) Colony formation assay in rodent cells treated with increasing doss of γ-irradiation. Linear-quadratic model was used to fit the survival data. Some cell lines showed a minimal quadratic component after fitting.

(G) LD50 of the rodent cells calculated from the linear-quadratic model fitting in (F). Error bars represent SEM (n = 3).

(H and I) LD50 significantly correlates with species maximum lifespan, but not body mass. r, Pearson correlation coefficient. p-values were determined by Student's t test for Pearson correlation.

(J) LD50 significantly correlates with NHEJ efficiency measured in Figure 2. r, Pearson correlation coefficient. p-values were determined by Student's t test for Pearson correlation.

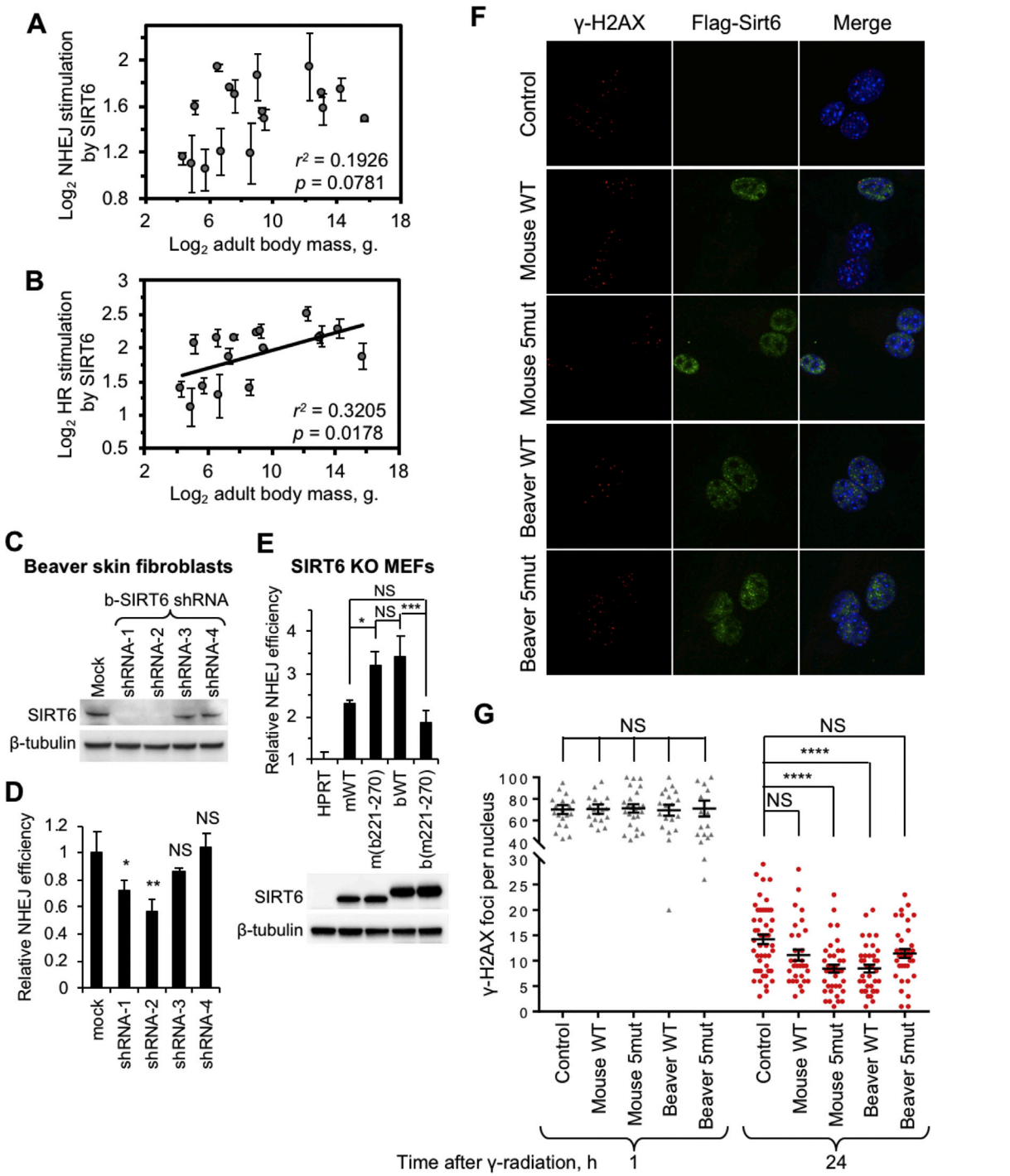

Figure S5. SIRT6 from Long-Lived Species Mediates More Efficient DSB Repair than SIRT6 from Short-Lived Species, Related to Figures 4 and 5

(A and B) SIRT6 ability to promote DSB repair does not correlate with adult body mass. The data from Figure 4 were used to test the correlation between SIRT6 ability to promote DSB repair and adult body mass of the corresponding species. (A) SIRT6 ability to promote NHEJ repair does not correlate with adult body mass. The conclusion holds true after phylogenetic correction (r^2 = 0.093, p = 0.23). (B) SIRT6 ability to promote HR repair significantly correlates with adult body mass. But the significance was lost after correction for phylogenetic non-independence (r^2 = 0.17, p = 0.10). Experiments for each SIRT6 were repeated at least three times. Error bars indicate SD *r*, Pearson correlation coefficient. p values were determined by Student's t test for Pearson correlation.

(C) Expression of SIRT6 in beaver skin fibroblasts after RNAi-mediated knockdown.

(legend continued on next page)

(D) DSB repair efficiency in SIRT6 knockdown cells generated in (C). Error bars indicate SD (n = 3). Statistical significance was determined using one-way ANOVA with Tukey's post hoc test.
(E) The region identified in Figure 5B showed similar results in SIRT6 knockout MEF cells. Error bars indicate SD (n = 3). Statistical significance was determined using one-way ANOVA with Tukey's post hoc test.
(F) Representative fluorescent micrographs of cells stained for Flag-SIRT6 and γ-H2AX. SIRT6 knockout MEFs expressing different SIRT6 proteins at 24 h after 8 Gy of γ-irradiation are shown.
(G) Quantification of γ-H2AX foci in Flag-SIRT6 positive cells at 1 h and 24 h after 8 Gy of γ-irradiation. Error bars indicate SEM (n > 30). Statistical significance was determined using one-way ANOVA with Tukey's post hoc test.
NS, not significant; *$p < 0.05$, **$p < 0.01$; ***$p < 0.001$, ****$p < 0.0001$.

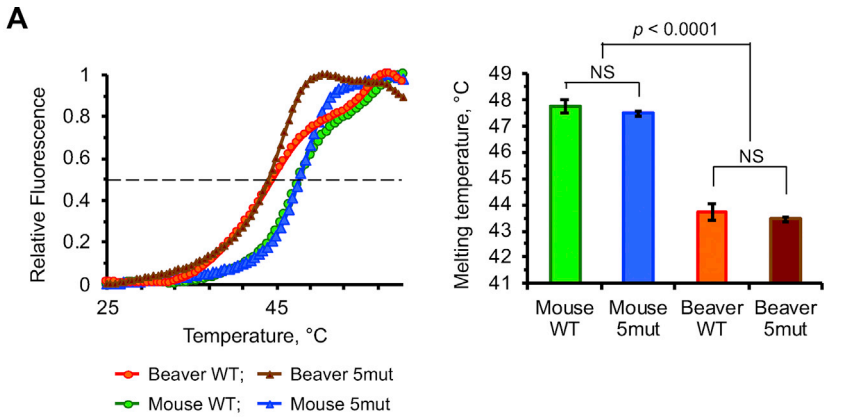

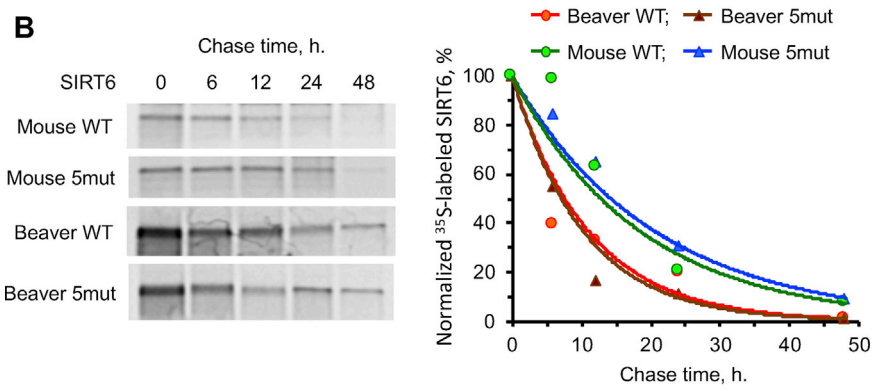

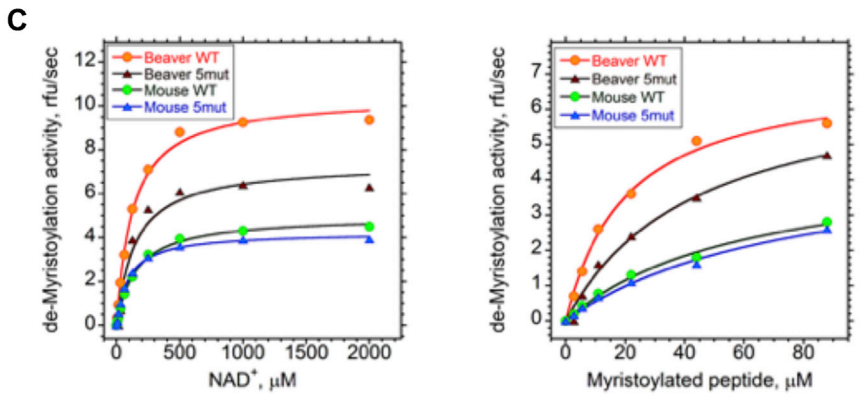

	Km NAD$^+$ (µM)	Vm (rfu/sec)	Vm/Km
Beaver WT	138.6 ± 10.6	10.4 ± 0.25	0.075
Beaver 5mut	144.6 ± 35.8	7.3 ± 0.5	0.05
Mouse 5mut	96.0 ± 5.2	4.3 ± 0.1	0.045
Mouse WT	150.9 ± 9.6	5.0 ± 0.1	0.033
	Km Myristoylated peptide (µM)	**Vm (rfu/sec)**	**Vm/Km**
Beaver WT	21.3 ± 2.1	7.4 ± 0.3	0.347
Beaver 5mut	43.7 ± 9.1	7.0 ± 0.7	0.16
Mouse 5mut	77.2 ± 14.6	4.7 ± 0.5	0.061
Mouse WT	60.0 ± 9.8	4.6 ± 0.4	0.077

(legend on next page)

Figure S6. Biochemical Characterization of the Mouse and Beaver SIRT6 Proteins, Related to Figure 6

(A) Thermal stability of the mouse and beaver SIRT6 proteins is not determined by the five amino acid changes. Left, representative thermal stability curves for mouse WT, mouse 5mut, beaver WT, and beaver 5mut SIRT6 proteins. The cross points with the horizontal line indicate the melting temperature (Tm) for each protein. Tm was measured by the incorporation of SYPRO orange dye to the protein while it is denaturing. Right, melting temperature of mouse WT, mouse 5mut, beaver WT, and beaver 5mut proteins calculated from the thermal stability curves. The experiment was repeated three times and error bars represent SD Statistical significance was determined by one-way ANOVA with Tukey's post hoc test.

(B) Left, autoradiography images of the SIRT6 proteins from the pulse chase assays. Radiolabeled cells were harvested at indicated time points during the chase period and subjected to immunoprecipitation using a SIRT6 antibody. Right, radioactive intensities were quantified from the gels on the left and fitted by exponential functions.

(C) Kinetic parameters (K_m and V_m) of mouse WT, mouse 5mut, beaver WT, and beaver 5mut SIRT6 proteins' de-myristoylation activities. Details of the assays are described in Methods. Each individual rate is based upon the average of triplicate kinetic measurements and rates showed excellent agreement (less than 5% error).

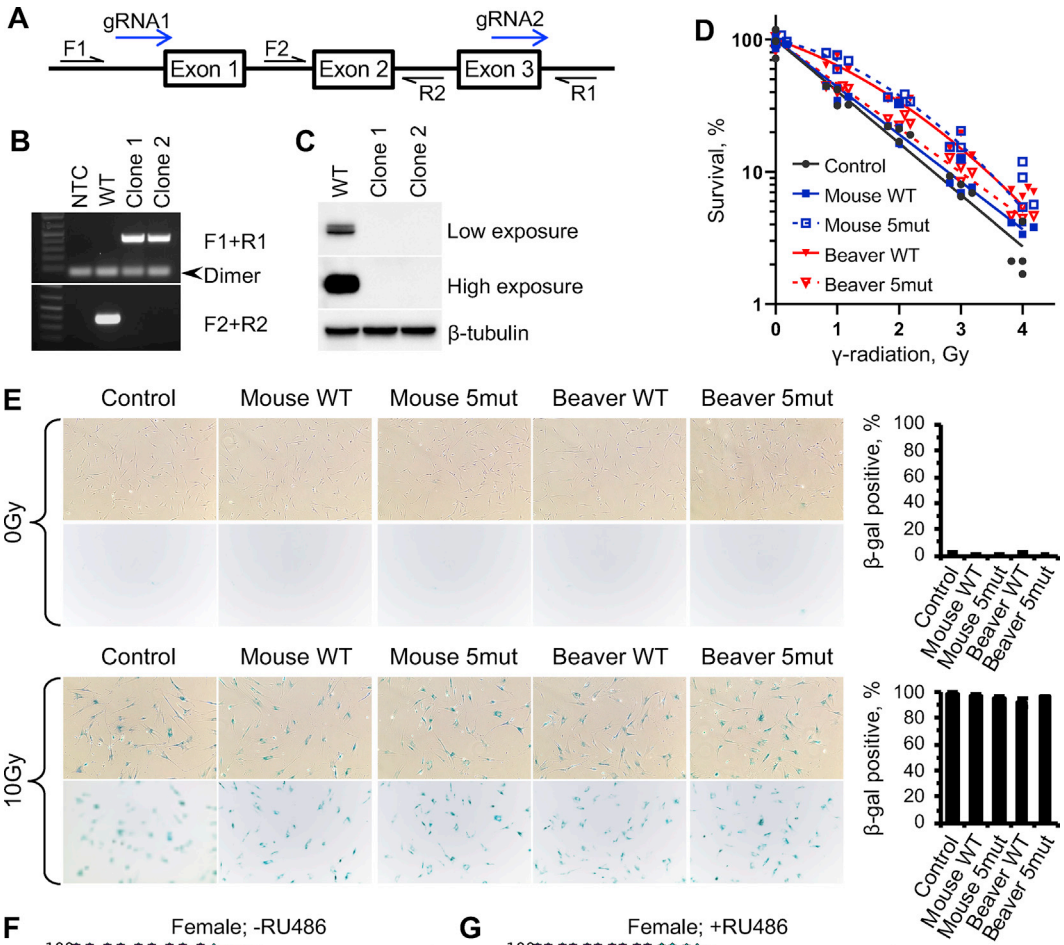

H

Genotypes	RU486	n	Median lifespan (Days)	Change %	Maximum lifespan (Days)	Change %	*p*-value Log Rank	*p*-value Wilcoxon
Control	–	353	63	-	77	-	-	-
Mouse WT	–	360	63	0%	78	1.3%	NS	NS
Mouse 5mut	–	341	64	1.6%	80	3.9%	NS	NS
Beaver WT	–	339	63	0%	80	3.9%	NS	NS
Beaver 5mut	–	348	63	0%	78	1.3%	NS	NS
Control	+	343	62	-	78	-	-	-
Mouse WT	+	365	68	**9.7%**	84	**7.7%**	$<1.0\times10^{-10}$	$<1.0\times10^{-10}$
Mouse 5mut	+	359	70	**12.9%**	90	**15.4%**	$<1.0\times10^{-10}$	$<1.0\times10^{-10}$
Beaver WT	+	352	73	**17.7%**	92	**17.9%**	$<1.0\times10^{-10}$	$<1.0\times10^{-10}$
Beaver 5mut	+	355	69	**11.3%**	89	**14.1%**	$<1.0\times10^{-10}$	$<1.0\times10^{-10}$

(legend on next page)

Figure S7. Stronger SIRT6 Leads to a Longer Lifespan, Related to Figure 7

(A) Strategy to generate SIRT6 knockout human dermal fibroblasts. gRNA, guide RNAs used to generate deletion of exons 1-3 using CRISPR-Cas9. The primers to confirm deletion of exons 1-3 are indicated.

(B) PCR to confirm the deletion of exons 1-3 of SIRT6 in independent clones.

(C) western blot to confirm the CRISPR knockout of SIRT6.

(D) Colony formation assay in SIRT6 knockout dermal fibroblasts expressing different SIRT6 proteins. Linear-quadratic model was used to fit the survival data. Some cell lines showed a minimal quadratic component after fitting.

(E) Representative images and quantification of SA β-gal positive cells after 0 Gy and 10 Gy of γ-irradiation.

(F and G) Stronger SIRT6 leads to a longer lifespan in female *Drosophila*. The results of the female flies from the same experiment as in Figures 7E–7F are presented.

(H) Summary of the parameters and statistics of the lifespan measurement. Survival data was analyzed using OASIS 2.